JM PAPERS

Influence of slip velocity in a two-phase bubbly jet

Hyunduk Seo[1], Goran Marjanovic[2], S. Balachandar[2] and Kyung Chun Kim[1],†

[1]School of Mechanical Engineering, Pusan National University, Busan 46241, Republic of Korea

[2]Department of Mechanical and Aerospace Engineering, University of Florida, Gainesville, FL 32611, USA

The effect of the slip velocity in a bubbly jet ($Re = 3000$, initial void fraction $= 1.1\%$) is studied with various bubble slip ratios (0.07–2.1 times the inlet velocity, 0.01–0.31 m s^{-1} in dimension). The governing equations, which are the conservation of mass, momentum and volume fraction, are solved by direct numerical simulations. A set of ordinary differential equations was derived by using a conventional one-dimensional integral framework on jets and by expressing the slip velocity using an exponential function. The one-dimensional analysis of bubbly jets successfully predicted the jet velocity radius, centreline velocity and the gas spread rate downstream of the bubbly jet. Second- and third-order statistics were also analysed to better understand the turbulent characteristics of the bubbly jet. A high slip ratio results in a rigid, narrower bubbly jet core region, where the turbulent kinetic energy is conserved along the centreline but does not diffuse towards the ambient region. The narrow, circular region around the core at high slip ratios decreased the turbulent kinetic energy. In the rigid bubbly jet core, turbulent diffusion of the gas phase is suppressed and has low correlations with the velocity fluctuations. Turbulence characteristics such as turbulence stress were compared with single-phase jet and plume results from existing literature. The magnitude of the turbulence characteristics at the lowest slip ratio is comparable with what is found in the literature, but there is a rapid transition from slip ratios of 0.14 to 0.7. Furthermore, the turbulent kinetic energy budget was analysed for each case. The production term had the largest contribution, and its magnitude was almost five times the buoyancy production downstream. High slip ratio cases show a positive peak of pressure strain and turbulent diffusion along the centreline.

Key words: gas/liquid flow, buoyant jets

1. Introduction

We typically refer to a bubbly plume as a plume that consists of water and air. If there is an initial momentum at the source of the plume, it can be referred to as a bubbly jet. In

† Email address for correspondence: kckim@pusan.ac.kr

a bubbly jet and plume, the existence of two different phases can enhance the transport of mass, momentum and energy without any moving mechanical parts. This advantage leads to a bubbly jet and plume being used in variety of engineering fields, such as destratification of a lake or river, wastewater treatment, chemical reactors and metallurgical processes (Shah *et al.* 1982; Milgram 1983; Wüest, Brooks & Imboden 1992; Asaeda & Imberger 1993; Jobehdar *et al.* 2016).

In the early stage of jet and plume studies, most researchers focused on the integral model, which was inspired by experimental observation and theory on a thermal plume by Schmidt (1941) and developed by Morton, Taylor & Turner (1956). The integral model on the thermal plume of Morton *et al.* (1956) is given by making several critical assumptions: (1) the main body of the flow is incompressible but the ambient fluid is stratified; (2) self-similarity of the plume velocity and buoyancy profiles; and (3) the rate of entrainment at each height is proportional to the centreline velocity at the same height. The assumptions have been extended to bubbly flows and the assumptions for the bubbly flows will be discussed later.

Bubbly plumes have attracted much attention because of their numerous applications, especially in the fields of offshore and ocean engineering. Early analytical studies on a bubbly plume were conducted to investigate their ability as a break water and a conditioning system for melting ice in the Arctic area (Taylor 1955; Ince 1964). Taylor (1955) and Evans (1955) analysed the velocity potential of an entrained flow and a surface current result from bubbly plumes. The bubbly plume was assumed to consist of very fine bubbles under the restriction of relative motion of bubbles. Kobus (1968) showed that the velocity profile of the bubbly plume satisfied a Gaussian distribution by using an experimental investigation. Ditmars & Cederwall (1974) recast the conservation equations of Morton *et al.* (1956) and proposed an analytical model by applying the assumptions that bubbles have a constant relative velocity (slip velocity) and spreading ratio between each phase. The analytical model was verified with the case of a large scale bubbly plume from Kobus (1968). The proposed model showed that the centreline axial velocity of the bubble plume was inversely proportional to the slip velocity and the entrainment coefficient. Milgram (1983) suggested semiempirical functions of an amplification factor of the momentum and an entrainment coefficient correlated with the local bubble Froude number, but the slip velocity and spreading ratio between water and bubbles are considered to be constant.

Lima Neto (2015) refined the results from the experimental study on bubbly jets with a wide range of Reynolds number and void fraction by Lima Neto, Zhu & Rajaratnam (2008). The entrainment coefficient, amplification factor of the momentum and spreading ratio were calculated between each phase by using the least squares approximation. The slip velocity was predicted as a function of the size of the bubble. The (above) coefficients derived by Lima Neto (2015) were substituted into bubbly jet conservation equations to calculate integral parameters such as the axial velocity of each phase and the concentration of bubbles. However, the limitations of Lima Neto (2015) are as follows. (1) The governing equation regards the entrainment coefficient as a constant for the entire flow field. In other words, the variation of the entrainment coefficient as the bubbly jet evolve, which has been reported by Priestley & Ball (1955), List (1982) and Milgram (1983), is not considered. (2) The contribution of the bubble slip velocity on the buoyancy flux is included but the spreading ratio, which can vary with slip velocity, is not considered (Socolofsky & Adams 2005). The limitations listed above should be solved for the engineering application of the integral approach to bubbly jets.

Detailed flow structures and turbulence characteristics of a bubbly jet and plume have been investigated by many researchers. Mcdougall (1978) showed, from an experimental

observation, that the bubble plume consists of a central core with rising bubbles (inner circular plume) and an outer part with a spreading liquid phase into the surroundings (outer annular plume). Sun & Faeth (1986) and Bryant, Seol & Socolofsky (2009) used laser Doppler velocimetry and particle image velocimetry, respectively, to investigate turbulence properties such as turbulent stresses of bubbly jets and plumes.

Recently, Lai & Socolofsky (2019) used acoustic Doppler velocimetry to calculate the turbulent kinetic energy (TKE) budget of weak bubble plumes. However, the difference of refractive index between air and water remains as a difficulty in the experimental study of a bubbly jet and plume. Morphological irregularity of bubbles in a bubble plume remains a major obstacle and objective in both experimental and numerical studies (Santarelli, Roussel & Fröhlich 2016; Reichardt, Tryggvason & Sommerfeld 2017; Du Cluzeau, Bois & Toutant 2019). Therefore, the exact physical understanding of a bubbly jet and plume is still in question, and many researchers need to develop turbulent models.

Fabregat *et al.* (2015, 2016) conducted direct numerical simulations (DNS) of thermal, bubble and hybrid plumes with an Eulerian–Eulerian approach with the following assumptions: (1) bubbles are very fine; and (2) bubbles have constant slip velocity. The results showed that bubbles have an important role in the enhancement of turbulence.

The slip velocity must be assumed for the gas–liquid two-phase flow simulations. But the slip velocity is one of the important parameters, which can alter the overall structure of a bubble plume, as reported by Socolofsky & Adams (2005). Therefore, serious errors can result from an incorrect slip velocity, and slip velocity should be validated for simulations. Direct numerical simulation has high fidelity and is considered as the true solution of a flow field in a single-phase flow and is often used as a tool in turbulence model research. Recently, the application of DNS has been extended to multi-phase flow, especially solid–fluid two-phase flow (Reddy *et al.* 2013; Wu, Luo & Fan 2016; Akiki, Moore & Balachandar 2017) rather than gas–liquid two-phase flow.

The objective of the present study is the investigation of the influence of the slip velocity in bubbly jets. Various bubble slip ratios (0.07 to 2.1 times the inlet velocity) are considered and simulated with DNS. In the present study, particle-unresolved DNS is implemented such that macro- and mesoscales of the flow are fully resolved without additional closure models. However, the gas phase is dealt with as an active scalar with a slip velocity. In other words, additional particle–liquid interactions such as lift and drag are not realised in the simulation. Based on the DNS result, we derived a set of one-dimensional (1-D) equations that includes the effect of slip velocity. The effect of the slip velocity in the spreading ratio between the liquid and gas phases is introduced as an additional 1-D equation. The variation of the entrainment coefficient as the bubbly jet evolves is considered as Priestley & Ball (1955) and List (1982) suggested. The behaviour of bubbly jets with different slip velocities is analysed with turbulent statistics, in detail.

The paper is organised as follows. In § 2, we discuss methods used for the problem set-up and validation of the simulation. In § 3, we present results regarding instantaneous flow fields, 1-D analysis and turbulent statistics. In § 4, we discuss the conclusions.

2. Methods

2.1. *Problem set-up*

In this study, a bubbly jet is supplied with momentum from a round source of diameter D at the bottom of the computational domain (figure 1*a*). At the source, the fluid velocity and
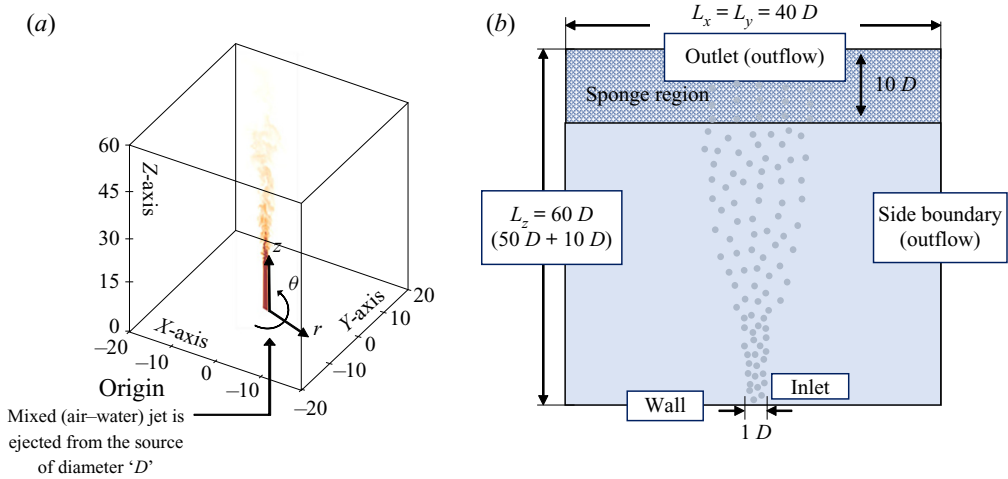
Figure 1. Schematic of the simulation: (*a*) nomenclature of the simulation; (*b*) boundary condition and domain size of the simulation.

gas concentration profiles are specified as hyperbolic tangent functions of radial position r:

$$U_z(r, 0) = U_{z0} \left[0.5 \tanh \left(\frac{0.5D - r}{0.05} + 1 \right) \right], \tag{2.1}$$

$$\Phi_b(r, 0) = \Phi_{b0} \left[0.5 \tanh \left(\frac{0.5D - r}{0.05} + 1 \right) \right], \tag{2.2}$$

where U_{z0} is the centreline velocity at the source and Φ_{b0} is the centreline gas concentration at the source. In the simulation, the centreline values at the source are used as the velocity and concentration scaling.

To derive the governing equations, we assume that (1) the bubbles have a constant axial slip velocity; (2) the flow is isothermal; (3) Boussinesq approximation applied; and (4) the contribution of the gas phase to the momentum of the flow is negligible. The constant axial slip velocity implies that bubbles in each simulation are monodispersed and relative lateral motions of bubbles are neglected. The concept of constant slip velocity is widely used in many numerical and experimental studies on bubbly jet and plumes and generally reflected as a drift velocity model in the scalar transport equation (Fabregat *et al.* 2015, 2016; Yang *et al.* 2016). In real bubbly jets, there might be very complex bubble breakup and coalescence processes, which can result in the change of bubble slip velocity. The bubble breakup and coalescence processes depend on several flow conditions such as turbulent dynamics, gas-phase properties and void fraction. In this study, the bubbly flow regime of the bubbly jet is controlled and physically equivalent to the discrete bubbly flow regime (very low superficial gas and liquid velocities) where the interactions between bubbles are negligible (Zhang *et al.* 1997). Boussinesq approximation implies that the density variation in the flow only affects the gravity term and appears as buoyancy forces in the momentum equation. It can be only applied due to the very low void fraction of the simulation in this study. Furthermore, the contribution of the gas phase to the momentum can be neglected because the contribution is much lower than buoyancy (Buscaglia, Bombardelli & García 2003), but a model to realise this effect costs too much due to more derivatives regarding the void fraction in the momentum equation (Sokolichin, Eigenberger & Lapin 2004). In fact, lift forces on bubbles do not have a negligible effect on the radial distribution

of bubbles (Fraga & Stoesser 2016). Especially, it is recently reported that the low-void fraction condition is more vulnerable to the modulation of the bubble population near the source of the bubbly jet (Seo & Kim 2021). In this study, to secure the appropriate condition for the proposed assumptions, and to investigate downstream flow characteristics of the bubbly jet, we keep the low-void fraction condition. The validation for downstream flow characteristics by comparison with experiment is shown in § 2.3. Governing equations for DNS are shown as

$$\nabla \cdot \boldsymbol{u} = 0, \tag{2.3}$$

$$\frac{\partial \boldsymbol{u}}{\partial t} + \boldsymbol{u} \cdot \nabla \boldsymbol{u} = -\nabla p + \frac{1}{Re}\nabla^2 \boldsymbol{u} + Ri\phi_b \hat{k}, \tag{2.4}$$

$$\frac{\partial \phi_b}{\partial t} + \nabla \cdot (\boldsymbol{u}\phi_b) = \frac{1}{Pe}\nabla^2 \phi_b - u_{sr}\frac{\partial \phi_b}{\partial z}, \tag{2.5}$$

where $Re = (\rho_l U_{z0} D)/\mu_l$, $Ri = (g\beta\Phi_{b0}D)/(U_{z0}^2)$, $Pe = (DU_{z0})/\mathcal{D}$, $u_{sr} = u_{slip}/U_{z0}$ and $\beta = (\rho_l - \rho_b)/\rho_l$. Here ρ is the density, μ is the dynamic viscosity, g is the non-dimensionalised gravitational acceleration ($g = g^*D/U_{z0}^2$, g^* is the gravitational acceleration), $\mathcal{D}$ is the diffusion coefficient, u_{slip} is the slip velocity and u_{sr} is the slip ratio. In this study, governing equations of each phase are based on the two-fluid model with the Eulerian–Eulerian approach. The gas phase velocity is modelled with the drift velocity and the slip velocity appearing in only the axial component.

The last equation is non-dimensionalised with the inlet void fraction, Φ_{b0}, as the void fraction scale. Therefore, $\boldsymbol{u}$, p and ϕ_b are non-dimensional velocity, pressure and gas concentration, respectively. Liquid and gas phases are denoted by l and b, respectively. In the present study, the turbulent Schmidt number (Sc_t), which is the ratio between the advective transport and the diffusive transport in turbulent flows, is chosen to be unity based on the assumptions that the effect of bubbles in the bubbly jet only appears as the buoyancy and slip velocity, and the gas concentration is regarded as an active scalar with buoyant force (Tominaga & Stathopoulos 2007; Combest, Ramachandran & Dudukovic 2011; Alméras *et al.* 2016). Therefore, the Péclet number, which is the product of the Reynolds number and the Schmidt number, is chosen to be the same as the Reynolds number. Specific parameters for each case are shown in table 1.

To conduct the grid independence test, the SR007 case was studied with a finer mesh, which is the SR007F case. Here Re is the Reynolds number, Pe is the Péclet number; L_x, L_y, L_z are the size of the domain along three directions; and N_x, N_y, N_z are the number of grid points. Simulation cases with different u_{sr} were considered to investigate the effect of the slip ratio in the bubbly jet: SR007 with $u_{sr} = 0.07$; SR014 with $u_{sr} = 0.14$; SR070 with $u_{sr} = 0.7$; SR140 with $u_{sr} = 1.4$; SR210 with $u_{sr} = 2.1$. This range of slip velocities is equivalent to 0.01–0.31 m s^{-1} in dimension. For a comprehensive understanding of the influence of bubble slip velocities in bubbly jets, we choose the value of 0.7 in the centre and sufficiently small (0.07 and 0.14) and substantially large (1.4 and 2.1) values. These slip velocities accord to bubbles which are several hundred micrometres in diameter from bubble aerators (Terasaka *et al.* 2011), and a few millimetres in diameter from porous media or spargers (Seol *et al.* 2007), and piped under deep springs (Milgram 1983). A single-phase jet case named 'Jet' was simulated as a benchmark.

Mesh quality	Fine		Coarse					
Case name	SR007F	Jet	SR007	SR014	SR070	SR140	SR210
Re	3000	3000	3000	3000	3000	3000	3000
Pe	3000	—	3000	3000	3000	3000	3000
Φ_{b0}	0.011	—	0.011	0.011	0.011	0.011	0.011
β	0.999	—	0.999	0.999	0.999	0.999	0.999
u_{sr}	0.07	—	0.07	0.14	0.7	1.4	2.1
$L_x \times L_y \times L_z$	$40 \times 40 \times 60$	$40 \times 40 \times 60$	$40 \times 40 \times 60$	$40 \times 40 \times 60$	$40 \times 40 \times 60$	$40 \times 40 \times 60$	$40 \times 40 \times 60$
$N_x \times N_y \times N_z$	$441 \times 441 \times 661$	$361 \times 361 \times 541$	$361 \times 361 \times 541$	$361 \times 361 \times 541$	$361 \times 361 \times 541$	$361 \times 361 \times 541$	$361 \times 361 \times 541$

Table 1. Flow parameters and computational domain for simulation.

2.2. *Numerical method*

The governing equations were solved using the spectral element code Nek5000, which has been extensively validated (Fischer, Lottes & Kerkemeier 2008; El Khoury *et al.* 2013; Salehipour, Peltier & Mashayek 2015; Tammisola & Juniper 2016). The computational domain is shown in figure 1(*b*). The outflow condition at the top is a Neumann boundary condition with zero gradient of the velocity and active scalar. At the bottom, a Dirichlet boundary condition with zero velocity and active scalar is applied, except at the inlet. The computational domain is discretised with $40 \times 40 \times 60$ elements.

The clustered grid extends from the origin toward the boundaries with an expansion ratio of 1.025, (i.e. $\Delta x_{i+1}/\Delta x_i = 1.025$). Within each element are non-uniform Gauss–Lobatto–Legendre points of polynomial order 9. For the grid convergence test, a polynomial order of 11 is applied to the case with $u_{sr} = 0.07$ (SR007). The side boundaries are far enough away from the jet in order to avoid bounding effects on the entrainment and recirculation regions of the jet. A fully developed bubbly jet is ensured by running each case at least 28 time units ($\tau = H/U_{z0}$, where H is the height of the computational domain), which is equivalent to 700 000 time steps. Turbulent statistics are calculated by averaging over 400 000 time steps.

At the top boundary there is a sponge region where the viscosity of the fluid is linearly increased as the fluid reaches the boundary. It is expected that forming a pseudoflow domain with increasing viscosity can reduce severe disturbances at the boundary. For downstream of the jet ($z/D = 50$–60), the viscosity is linearly increased by up to 50 times. This scheme has a higher computational cost in the sponge region downstream of the domain, but it can reduce the overall computational cost for treatment on the top side of the domain via other methods. Furthermore, it ensures the stability of the simulation.

2.3. *Validation of simulation*

A case without the bubble phase, Jet, was simulated to validate the numerical method and to quantitatively analyse the effect of the gas phase. This case has a single-phase jet with a Reynolds number of 3000. The asymptotic decay characteristic and point source are explicitly expressed as follows (George 1989):

$$\frac{U_{z0}}{U_{zc}} = \frac{1}{B_u}\left[\frac{z}{D} - \frac{z_0}{D}\right], \quad (2.6)$$

where U_{zc} is the mean axial centreline velocity, B_u is the decay constant and z_0 is the virtual origin.

Figure 2(*a*) shows the decay of the jet from several case studies. The jet studied by Taub *et al.* (2013) has a decay constant of 5.56, which is in the range of 5.7 to 6.1 where most decay constants in the literature were observed (Wygnanski & Fiedler 1969; Rodi 1975; Panchapakesan & Lumley 1993). It is lower than the decay constant of the present jet case, even though the jet of Taub *et al.* (2013) has similar numerical conditions to the present work. The discrepancy occurs due to the inlet velocity profile. The inlet velocity profile of Taub *et al.* (2013) is a top-hat profile. On the other hand, smooth inlet profiles were used in the present study, by Boersma, Brethouwer & Nieuwstadt (1998) and Ferdman, Ötügen & Kim (2000) (a hyperbolic tangent profile (§ 2.1) with a parabolic profile and a profile from a fully developed pipe flow, respectively). These result in higher decay constants than the ordinary decay constant of the jet. In the present study, the value of the virtual origin is much higher than other jets, and seems to be attributed to the fact that the present study has no perturbation at the inlet. The effect of an initial turbulence level on the length of
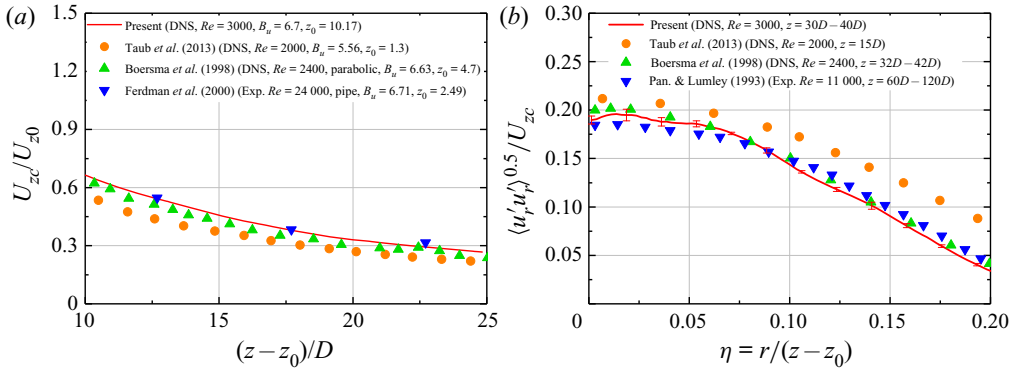
Figure 2. (*a*) Normalised centreline velocity with height. (*b*) Normalised radial turbulent intensity with non-dimensional radial coordinate η.

the zone of flow establishment (ZFE) is reported by Chen & Nikitopoulos (1979). They showed that a low initial turbulence level of a jet can make the length of ZFE two to three times longer than that of jets with a high initial turbulence level.

Figure 2(*b*) compares the radial variation of the turbulence intensity obtained at a downstream location in the flow. The radial variation of turbulence intensity is normalised by the centreline velocity. The present work shows a very similar intensity profile to those of Boersma *et al.* (1998) and Panchapakesan & Lumley (1993). Taub *et al.* (2013) has a slightly different profile from the others because the turbulence intensity profile was obtained from a height of $z = 15D$, which is closer to the virtual origin than in the present study.

A grid independence test was conducted for the case with $u_{sr} = 0.07$ with two different qualities of meshes, as shown in table 1. The quality of the mesh is controlled by changing the polynomial order. A polynomial order 9 is the 'coarse' case, which is denoted as SR007, and a polynomial order 11 is the 'fine' case, which is denoted as SR007F. Figure 3(*a*) compares the jet velocity radius of bubbly jets. The jet velocity radius is obtained with a Gaussian-like velocity profile assumption of the radial distribution of the axial mean velocity. In the near field of the bubbly jet, each case shows a nearly identical value. In the far field of the bubbly jet, the velocity radius evolves with a slight oscillation in each case, but each case still shows similar values to each other. Root mean square error of the velocity radius of each case is 0.0042 where the height is $z = 10D{-}50D$. Figure 3(*b*) compares the time-averaged volume flux, momentum flux and buoyancy flux to show the effect of the quality of the mesh on the mean flow characteristics of the bubbly jet. The time-averaged mean volume flux, momentum flux, buoyancy and buoyancy flux of the flow are defined as follows:

$$Q(z) = 2\pi \int_0^\infty U_z(r, z)\, r\, \mathrm{d}r, \tag{2.7}$$

$$M(z) = 2\pi \int_0^\infty U_z^2(r, z)\, r\, \mathrm{d}r, \tag{2.8}$$

$$B(z) = 2\pi \int_0^\infty \beta g \Phi_b(r, z)\, r\, \mathrm{d}r, \tag{2.9}$$
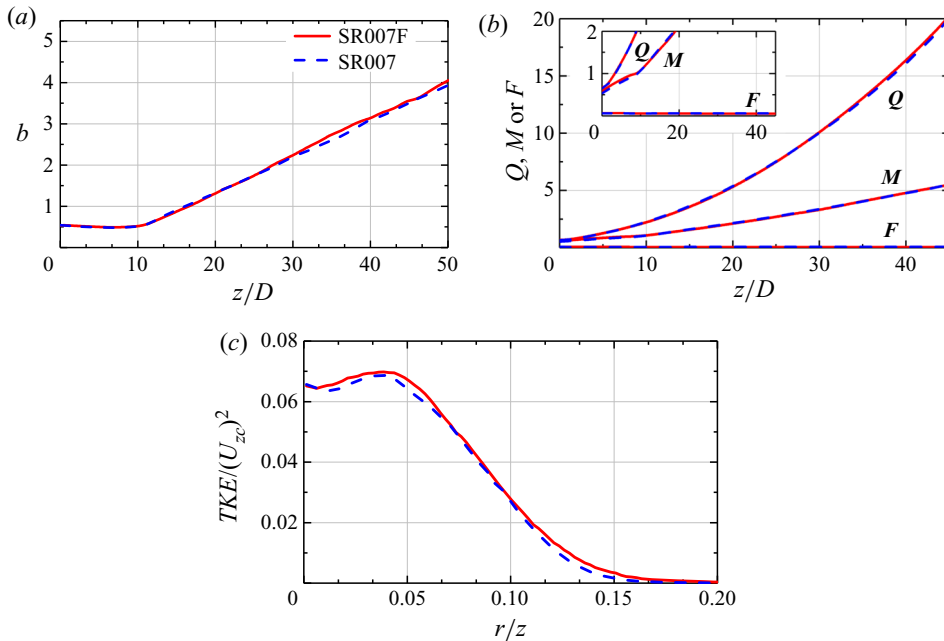
Figure 3. Result of grid independence test for 'coarse' and 'fine' mesh with $u_{sr} = 0.07$: (*a*) jet velocity radius based on the Gaussian-like velocity profile; (*b*) volume flux, momentum flux and buoyancy flux; (*c*) TKE at $z = 40D$.

$$F(z) = 2\pi \int_0^\infty \beta g(U_z(r, z) + u_{sr})\Phi_b(r, z)r \, \mathrm{d}r, \tag{2.10}$$

where U_z is the time-averaged axial velocity and Φ_b is the time-averaged gas concentration. The coarse and fine cases show similar profiles of mean flow characteristics as functions of height.

Figure 3(*c*) compares TKE at $z = 40D$. The coarse mesh shows a lower magnitude of TKE than the fine mesh. It appears that the lower spatial and temporal resolution could not resolve the small eddies in the jet. However, the coarse mesh case resolves the distinctive characteristics of the plume with good accuracy, such as the peak of TKE at the centreline and the off-centre peak around $r/z \sim 0.34$.

Comparison of the radial distribution of the TKE and Reynolds shear stress between the SR070 case and the bubbly jet, which was experimentally studied by Sun & Faeth (1986), is shown in figure 4. The SR070 case is chosen for comparison because SR070 case has a comparable slip velocity in dimension ($0.103 \, \mathrm{m \, s^{-1}}$) to the experiment ($0.108 \, \mathrm{m \, s^{-1}}$). The TKE in both cases shows very similar radial distributions and magnitudes downstream, and distinctive characteristics such as a peak along the centreline and an off-centre peak around $r/b \sim 0.38$. The Reynolds shear stress in both cases shows similar magnitudes and radial collapse toward the ambient. However, SR070 overestimated the shear stress in the core region. It is attributed to the fact that the present study does not consider drag forces that spread the bubbles outward, The absence of the drag force results in higher bubble concentration around the core region and promotes higher correlations between velocity fluctuations as analysed in the § 3.3. Based on the validations (figures 2–4), it seems that the simulation method in the present study can be used to implement DNS of the bubbly jet.
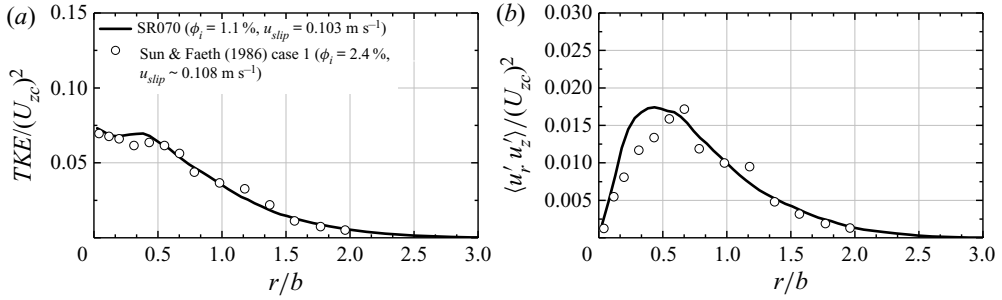
Figure 4. Comparison between SR070 case and bubbly jet experiment ($Re = 8740$, $z/D = 60$) conducted by Sun & Faeth (1986). The x-axis of the experimental data is reproduced by normalising with b, which is obtained with Gaussian-like velocity profile assumption of the radial distribution of the axial mean velocity of the experiment. (*a*) The radial distribution of the normalised TKE and (*b*) the radial distribution of the normalised Reynolds shear stress.
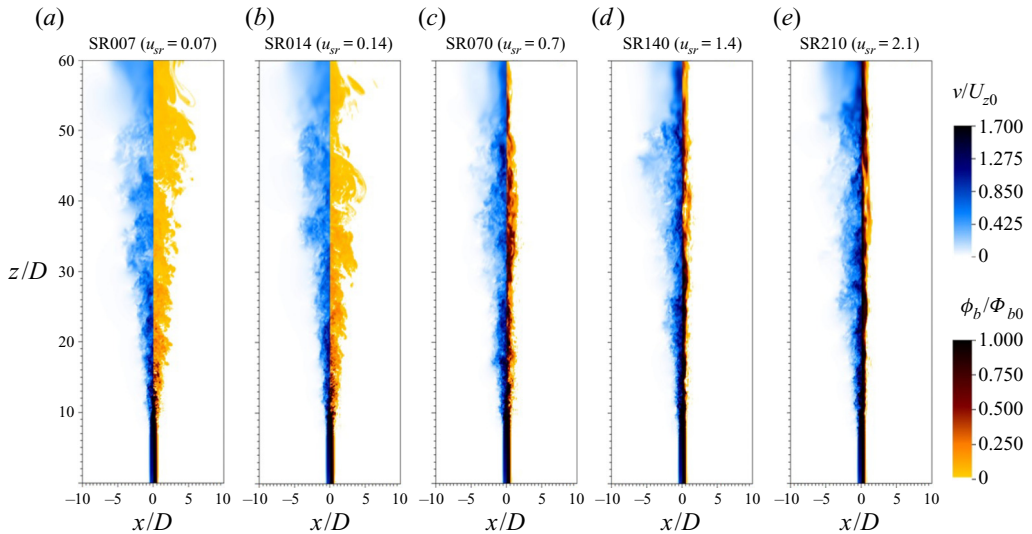

Figure 5. Instantaneous velocity magnitude and gas concentration fields of bubbly jets. The left-hand half and right-hand half of each plot show normalised velocity magnitude and gas concentration, respectively.

3. Results

3.1. *Instantaneous flow field*

Instantaneous velocity magnitude and gas concentration fields are shown in figure 5. The instantaneous velocity magnitude is defined as follows:

$$v = \sqrt{u_r^2 + u_\theta^2 + u_z^2}. \tag{3.1}$$

In the figure, the velocity magnitude and the gas concentration are normalised by the inlet axial velocity and inlet gas concentration, respectively. At the early stage of the flow ($0 < z/D < 10$), all cases accelerate and keep their potential core. But the potential core eventually collapses at $z/D \sim 10$, and both velocity magnitude and gas concentration start to be dispersed around $z/D \sim 10$. One of the salient differences between the cases with low slip ratio (LSR) and the cases with high slip ratio (HSR) is dispersion of the gas phase.
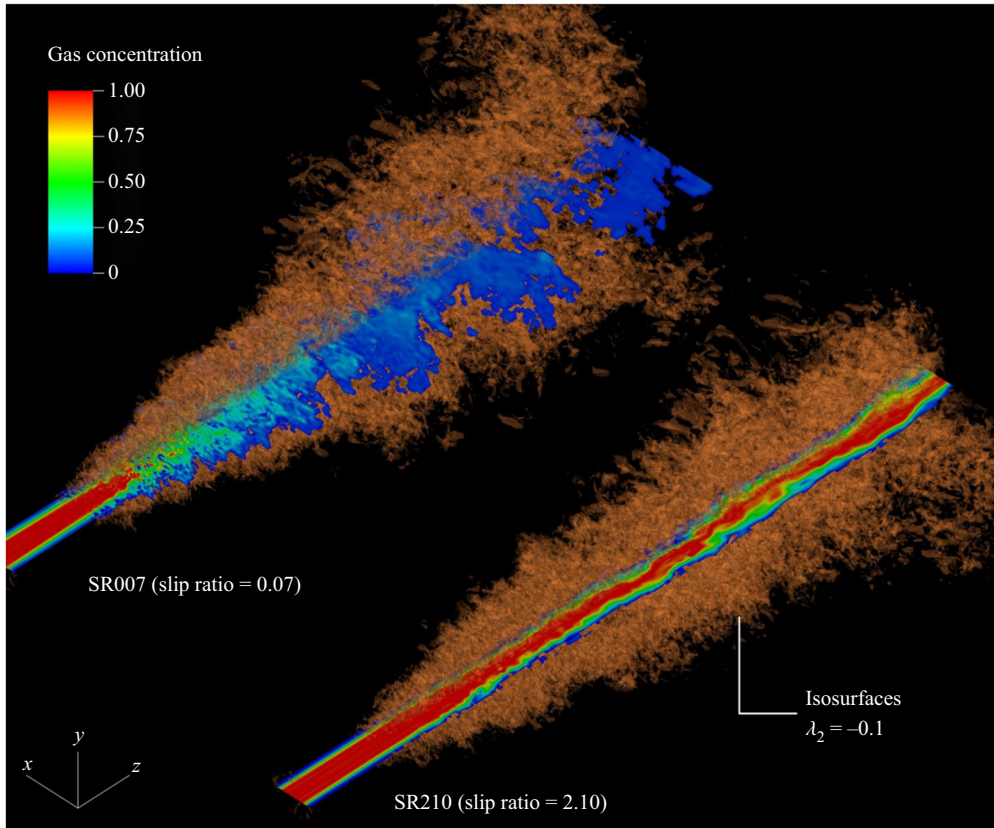
Figure 6. Gas concentration fields and isosurfaces of λ_2 vortices are shown for two different slip ratios, 0.07 and 2.1 (SR007 and SR210). The gas concentration contours of x–z plane are presented. Vortex structures are identified by using Lambda2 vortex criterion. Isosurfaces of vortex structures corresponding to $\lambda_2 = -0.1$ are presented.

The cases with $u_{sr} = 0.07$ and 0.14 (SR007 and SR014) show the dispersion of lumps of bubbles after the collapse of the potential core. Therefore, bubbles are discontinuously observed along the centreline. However, the cases with $u_{sr} = 0.7$, 1.4 and 2.1 (SR070, SR140 and SR210) show a rigid bubbly jet core region, which meanders with time. It results in a narrower spreading structure of the bubbly jet.

Figure 6 shows vortex structures and gas concentration of the cases with $u_{sr} = 0.07$ and $u_{sr} = 2.1$. The vortex is identified by using the Lambda2 vortex criterion (Jeong & Hussain 1995). The identified vortex in figure 6 seems to have more chaotic structures than those reported in many papers regarding jets (Becker & Massaro 1968; List 1982; Sarikurt & Hassan 2017) in terms of the presence of coherent structure such as a vortex ring and a horseshoe vortex. The vortical structures of the SR007 case are bounded around the interface between bubbles and ambient fluids. On the other hand, the vortical structures of the SR210 case show dense and narrower distribution. In both cases, vortex breakdown is universally observed by the collapse of the potential core.
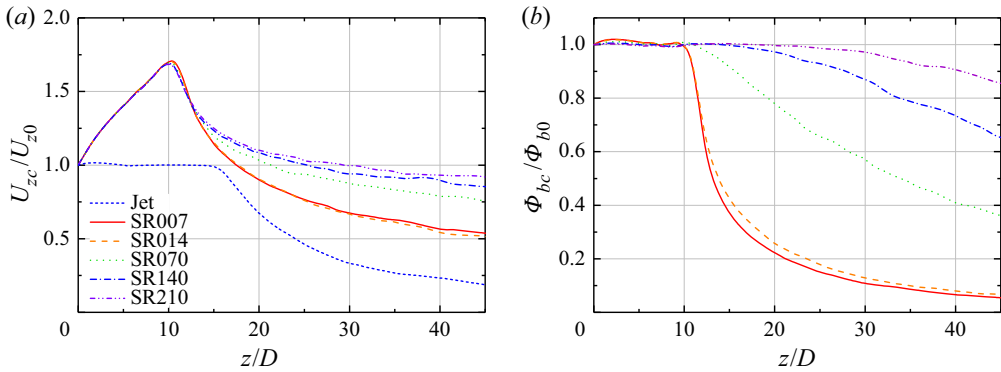
Figure 7. (*a*) Centreline velocity plotted as a function of downstream distance. (*b*) Centreline gas concentration plotted as a function of downstream distance.

3.2. *Integral frameworks with 1-D analysis*

In this section, the time averaged axial velocity, jet velocity radius and gas concentration radius will be defined and utilised as local variants (as functions of axial coordinate, z) of the 1-D model based on the assumption of Gaussian profiles to predict the evolution of the bubbly jet. Those local variants are obtained from our three-dimensional particle-unresolved DNS, where the bubbly jet naturally evolves and spreads with given viscosity and diffusivity (Reynolds number and Péclet number) in the governing equations (2.4) and (2.5). To reflect these natures in the 1-D model, two more closure models for the entrainment coefficient and spreading rate of gas phase are suggested and will be described in a further text.

The effect of slip velocity on the decaying characteristics of the axial velocity and gas concentration of the bubbly jet along the centreline are compared in figure 7. Figure 7(*a*) shows the centreline velocity normalised by the inlet velocity U_{z0}, and figure 7(*b*) shows centreline gas concentration normalised by the inlet gas concentration Φ_{b0}. As shown in figure 7, the presence of the gas phase accelerates the jet and keeps the gas concentration without dispersion up to $z = 10D$. Then, all cases with different slip ratios show a decay in the velocity. The single-phase jet, however, keeps its potential core up to $z = 15D$. Because the present study has no perturbation at the inlet, the presence of the gas phase results in earlier dispersion of the jet momentum and velocity acceleration until dispersion occurs farther downstream. It accords to the flow characteristics of buoyant jet (Chen & Nikitopoulos 1979; Henderson-Sellers 1983). It is reported that a lower Froude number condition (large difference between a jet initial temperature and an ambient temperature) of buoyant (thermal) jets results in a higher acceleration of the jet, and the length of the ZFE generally accords to the end of the acceleration. Also, it is reported that a higher Froude number results in an earlier acceleration.

Based on the assumption of a Gaussian profile and the ratio of conventional length scales between velocity and concentration profiles Morton *et al.* (1956), the jet velocity and gas concentration can be expressed as

$$U_z(r, z) = U_{zc} \exp(-r^2/b^2), \tag{3.2}$$

$$\Phi_b(r, z) = \Phi_{bc} \exp(-r^2/b_g^2), \tag{3.3}$$

$$b_g = \lambda b, \tag{3.4}$$

where U_{zc} is the time-averaged axial centreline velocity of the liquid, Φ_{bc} is the time-averaged centreline gas concentration, b is the $1/e$ width of the liquid velocity (jet velocity radius), b_g is the $1/e$ width of the bubble concentration (jet concentration radius) and λ is the spreading ratio between the bubble concentration and liquid velocity radius. These equations imply that integral properties of the bubbly jet are axisymmetric. From the Gaussian profile assumption, we can derive the volume flux, momentum flux and buoyancy flux as follows:

$$Q(z) = 2\pi \int_0^\infty U_{zc} \exp(-r^2/b^2) r \, dr = \pi U_{zc} b^2, \tag{3.5}$$

$$M(z) = 2\pi \int_0^\infty U_{zc}^2 \exp(-r^2/b^2) r \, dr = \frac{\pi U_{zc}^2 b^2}{2}, \tag{3.6}$$

$$B(z) = 2\pi \int_0^\infty \beta g \Phi_{bc} \exp(-r^2/(\lambda b)^2) r \, dr = \pi g' \Phi_{bc} \lambda^2 b^2, \tag{3.7}$$

$$F(z) = 2\pi \int_0^\infty \beta g (U_{zc} \exp(-r^2/b^2) + u_{sr}) \Phi_{bc} \exp(-r^2/(\lambda b)^2) r \, dr$$
$$= \pi g' \Phi_b \lambda^2 b^2 \left(\frac{U_{zc}}{1 + \lambda^2} + u_{sr} \right), \tag{3.8}$$

where g' is the reduced gravity ($g' = \beta g$). In figure 8, the DNS results for the bubbly jets with LSR show good agreement with the Gaussian distributions of the velocity and concentration profiles at all downstream distances. At the height of transition ($z = 10D$), all bubbly jets cases still show discrepancy from the Gaussian profiles regarding the velocity and gas concentration. However, cases with HSR still show discrepancy from the Gaussian profiles farther downstream ($z = 20D$). It is different from the report on buoyant jets by Chen & Nikitopoulos (1979). In buoyant jets, at the end of ZFE, the potential core of the jet will be eroded by the shear, and the radial distribution of the velocity and buoyancy seems to be Gaussian-like profiles. In the present study, the Gaussian-like distribution of the velocity and gas concentration profile of HSR cases appears around $z = 30D$.

From the Gaussian profile assumption, the jet conservation equations, which satisfy entrainment assumption of Morton *et al.* (1956), are derived as follows:

$$\frac{d(\pi U_{zc} b^2)}{dz} = 2\pi \alpha U_{zc} b, \tag{3.9}$$

$$\frac{d(\pi U_{zc}^2 b^2)}{dz} = \pi g' \Phi_{bc} (\lambda b)^2. \tag{3.10}$$

Equation (3.9) represents the entrainment of ambient fluid into the mean flow of the bubbly jet. Equation (3.10) represents the momentum balance of the bubbly jet. These equations can be rewritten in terms of the volume flux Q, momentum flux M and buoyancy B, respectively, as follows:

$$\frac{dQ_G}{dz} = 2\pi \alpha U_{zc} b, \tag{3.11}$$

$$\frac{dM_G}{dz} = B_G. \tag{3.12}$$

The subscript G indicates the Gaussian profile assumption. From (3.9) and (3.10), we can derive the following two ordinary differential equations regarding b and U_{zc} as functions
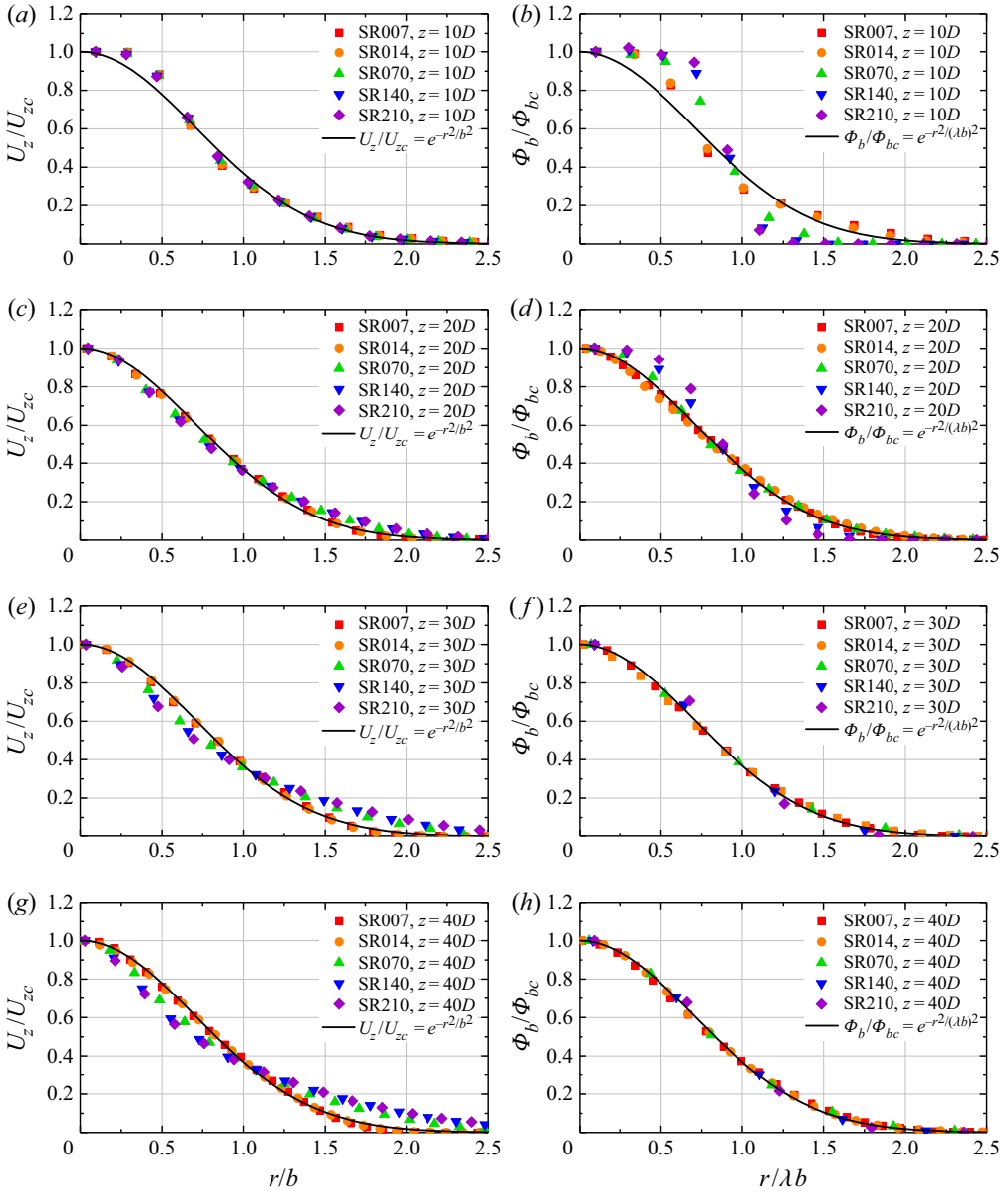
Figure 8. Velocity and gas concentration profile with different height. Velocity profiles at $z = 10D, 20D, 30D, 40D$ (a,c,e,g) and gas concentration profiles at $z = 10D, 20D, 30D, 40D$ (b,d,f,h).

of z:

$$\frac{\mathrm{d}}{\mathrm{d}z}(U_{zc}) = \frac{-2\alpha U_{zc}}{b} + \frac{2Q_g g'}{\pi U_{zc}/(1+\lambda^2) + u_{sr}} \frac{1}{U_{zc}b^2}, \tag{3.13}$$

$$\frac{\mathrm{d}}{\mathrm{d}z}(b) = 2\alpha - \frac{Q_g g'}{\pi U_{zc}/(1+\lambda^2) + u_{sr}} \frac{1}{U_{zc}b}; \tag{3.14}$$
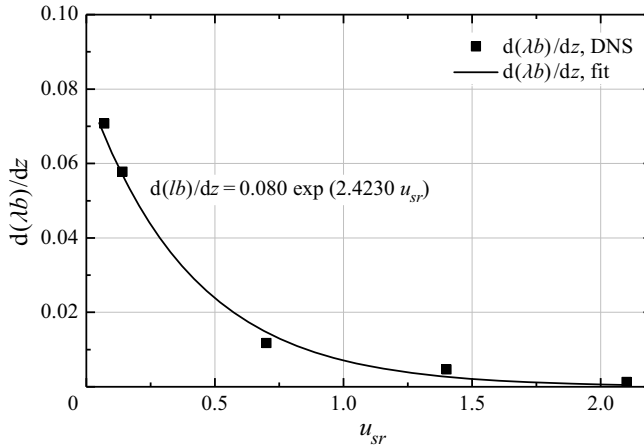
Figure 9. A curve fitting with an exponential function for each slip ratio case by an assumption that λb is a linear function of z.

the derivation is shown in appendix A. The bubble concentration radius, λb, can be expressed as an exponential function, as follows:

$$\frac{\mathrm{d}}{\mathrm{d}z}(\lambda b) = \eta_g \exp(-\gamma_{\lambda b} u_{sr}), \tag{3.15}$$

where η_g is the spread rate of the gas phase without any slip velocity in jets.

In buoyant jet experiments, the spread of scalars such as temperature and passive tracers is regarded to be proportional to only the spread rate η_g and ranges from 0.101 to 0.156 based on the source condition in previous studies (Fiscehr *et al.* 1979; Wang & Law 2002). In other words, there are no reports on the exponential term of the equation (3.15). In the present study, we considered one more coefficient, $\gamma_{\lambda b}$, which is a measure of the effect of the slip ratio of the gas phase. Equation (3.15) shows that the spread of the gas phase exponentially decreases as the slip ratio increases. In the present work, the rate of spread of the gas phase with height is plotted with slip ratio as shown figure 9. It is found that $\eta_g = 0.080$, which is smaller than what was found in the literature, and $\gamma_{\lambda b} = 2.423$.

There is an important parameter in the three ordinary differential equations, the entrainment coefficient α. It can be defined as a constant or as a function of other local variables (Morton *et al.* 1956). There have been several efforts to define the local entrainment coefficient because it varies significantly as the bubbly plume develops downstream (Kobus 1968; Ditmars & Cederwall 1974; Milgram 1983). To define the entrainment coefficient as a local function, Priestley & Ball (1955) and List (1982) suggested using the local Richardson number to define the local entrainment coefficient as follows:

$$\alpha = \alpha_j - (\alpha_j - \alpha_p)\left(\frac{R}{R_p}\right)^2, \tag{3.16}$$

where α is the local entrainment coefficient, which varies with height, α_j is the entrainment coefficient in the jet-like region, α_p is the entrainment coefficient in the plume-like region, R is the local Richardson number and R_p is the Richardson number in the plume-like region. The Richardson number represents the ratio between the buoyancy and inertia forces, which reflects the state of the plume in terms of flow development.
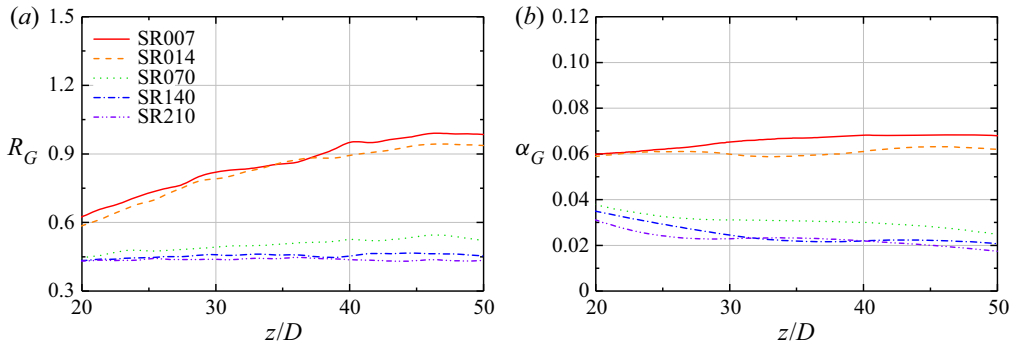
Figure 10. (*a*) Local Richardson number profile by Gaussian profile assumption $R_G = Q_G B_G / M_G^{(5/4)}$ and (*b*) local entrainment coefficient profile by Gaussian profile assumption with height $\alpha_G = (\mathrm{d}Q_G/\mathrm{d}z)/(2\pi b U_{zc})$.

Figure 10 shows the Richardson number and the entrainment coefficient. They are calculated based on the Gaussian profile assumption. The Richardson number of the higher slip ratio cases (SR140 and SR210) barely vary with height. This represents that a bubbly jet with a higher slip ratio encounters a limitation in the entrainment of ambient fluid earlier than a bubbly jet with a lower slip ratio. The entrainment coefficient of SR014 does not vary with height in the overall plume-like region. The entrainment coefficient at a lower slip ratio increases in the *z*-direction. In contrast, the entrainment coefficient at a higher slip ratio decreases in the *z*-direction.

The two jet characteristics in figure 10 show monotonic behaviour with respect to the height. Priestley & Ball (1955) and List (1982) related the monotonic behaviour of the entrainment coefficient and Richardson number by introducing the equation (3.16). Therefore, we replaced entrainment coefficients in the equations (3.13) and (3.14) with the equation (3.16) as in the study by Priestley & Ball (1955) and List (1982).

Next, we analysed the bubbly jet after the moment of collapse of the potential core ($z/D > 24$), i.e. zone of established flow. Direct numerical simulation results at $z/D = 24$ were used as the initial conditions of (3.13), (3.14), (3.15) and (3.16). Here α_j is assumed to be the same as the entrainment coefficient at $z/D = 24$ and α_p and R_j are assumed to be the values at $z/D = 50$.

Figure 11 shows a comparison between the DNS and the solution of the 1-D analysis. As shown in figure 11, the overall predictions shown with solid lines match the bubbly jet DNS results well. As shown in figure 11(*c*), the gas concentration width of the DNS result follows a linear exponential function (3.15). Figure 11(*d*) shows that the spreading ratio of the bubbly jet varies with height and ranges from 0.3 to 0.8 downstream. The results show agreement with the results of 0.66–0.69 from a weak bubbly plume experiment by Wang, Lai & Socolofsky (2019).

3.3. *Second-order statistics*

In this section, normalised second-order statistics of bubbly jets are presented to analyse the effect of slip velocity. The statistics are calculated from our three-dimensional particle-unresolved DNS results with governing equations (2.3), (2.4) and (2.5). Each velocity component (radial, azimuthal and axial velocities) and the gas concentration are decomposed into the mean and fluctuation as $u_r = U_r + u'_r, u_\theta = U_\theta + u'_\theta, u_z = U_z + u'_z$
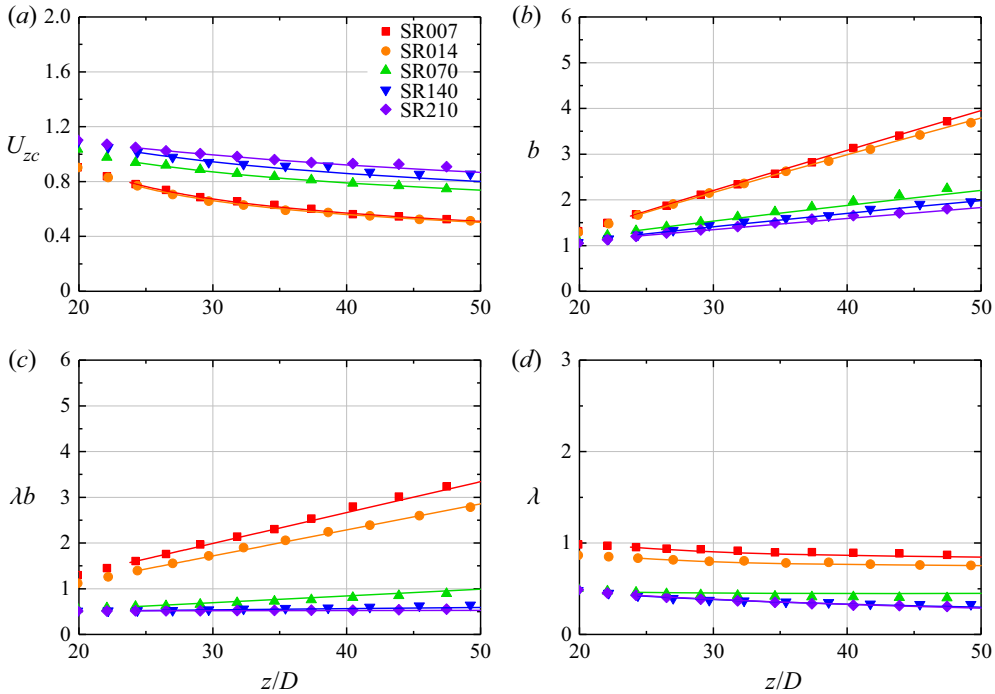
Figure 11. Comparison between 1-D analysis and DNS result: (*a*) centreline velocity; (*b*) jet velocity radius; (*c*) jet concentration width; (*d*) jet spread rate between gas and liquid (DNS result, symbols; 1-D solution, line).

and $\phi_b = \Phi_b + \phi'_b$. The time-averaged values such as the Reynolds normal and shear stresses are expressed as $\langle u'_r u'_r \rangle$ and $\langle u'_r u'_z \rangle$. Figure 12 shows the Reynolds normal stresses and shear stresses at $z = 20D$ (near field) and $z = 40D$ (far field). Each normal stress is normalised with the square of the centreline axial mean velocity.

In figures 12(*b*) and 12(*f*), the SR007 case shows that the magnitude of the radial and axial normal stresses reached 0.038 and 0.061, respectively. They are comparable with those of other jet cases: 0.04 and 0.053 (Boersma *et al.* (1998), round jet DNS); 0.036 and 0.067 (Wang & Law (2002), round buoyant jet experiment); and 0.034 and 0.058 (Panchapakesan & Lumley (1993), round jet experiment). This result shows that a very small slip velocity does not affect the magnitude of the TKE. But as the slip velocity increases, there are significant differences in the turbulence stress distribution.

It is observed that HSR cases (SR070, SR140 and SR210) have a steep collapse of normal stresses with the radial direction. However, LSR cases (SR007 and SR014) have more Gaussian-like distributions. In the far field, it seems that a HSR promotes rapid collapse, which is consistent with the collapse of the mean axial velocity profile in § 3.2. The radial normal stresses show a peak along the centreline.

An inflection point of the radial normal stress profile is universally observed in the bubbly jet core region. However, steepness around the inflection point varies with slip ratio. Particularly, LSR cases have much flatter and gentle profiles in the bubbly jet core region. The azimuthal and axial normal stresses show similar radial variation, which consists of a peak along the centreline and an off-centre peak. The radial variation of the azimuthal and axial normal stresses varies with the slip ratio in the same way as the variation of the radial normal stress varies.
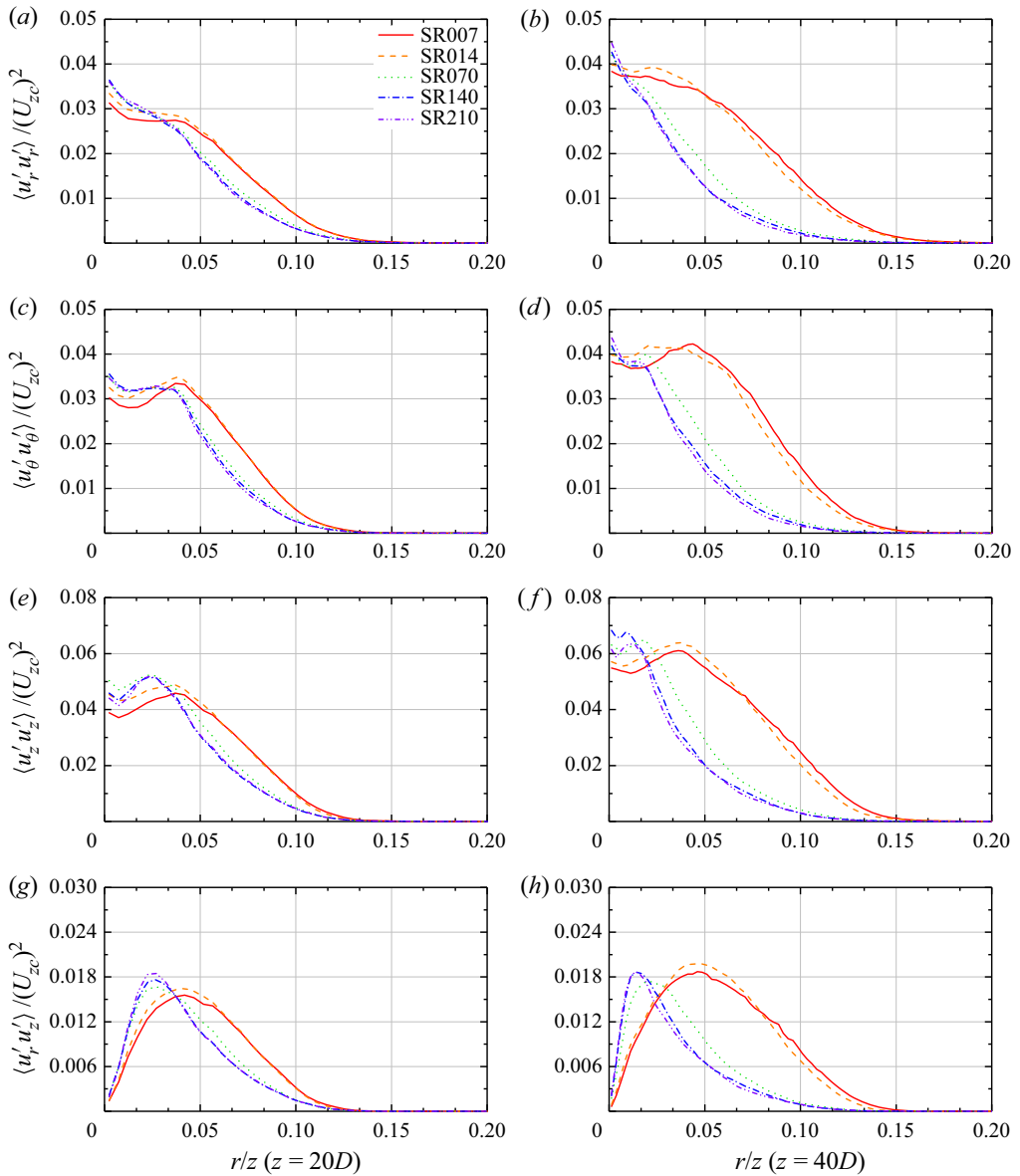
Figure 12. Reynolds normal stresses and shear stresses of bubbly jet with different slip ratios: (*a*) radial normal stress at $z = 20D$; (*b*) radial normal stress at $z = 40D$; (*c*) azimuthal normal stress at $z = 20D$; (*d*) azimuthal normal stress at $z = 40D$; (*e*) axial normal stress at $z = 20D$; (*f*) axial normal stress at $z = 40D$; (*g*) shear stresses at $z = 20D$; (*h*) shear stresses at $z = 40D$.

Figure 12(*g*) shows the Reynolds shear stress at $z = 20D$. The off-centre peak with the highest slip ratio (SR210) reached a value of 0.018, which is regularly observed in the far field of the jet in the literature (Panchapakesan & Lumley 1993; Boersma *et al.* 1998). Low slip ratio cases, however, have off-centre peaks at 0.015 at $z = 20D$ yet. In the far field ($z = 40D$), the HSR cases keep the magnitude of their Reynolds shear stress, but they skew to the centreline more (figure 12*h*). Although the peaks of SR007 and SR070
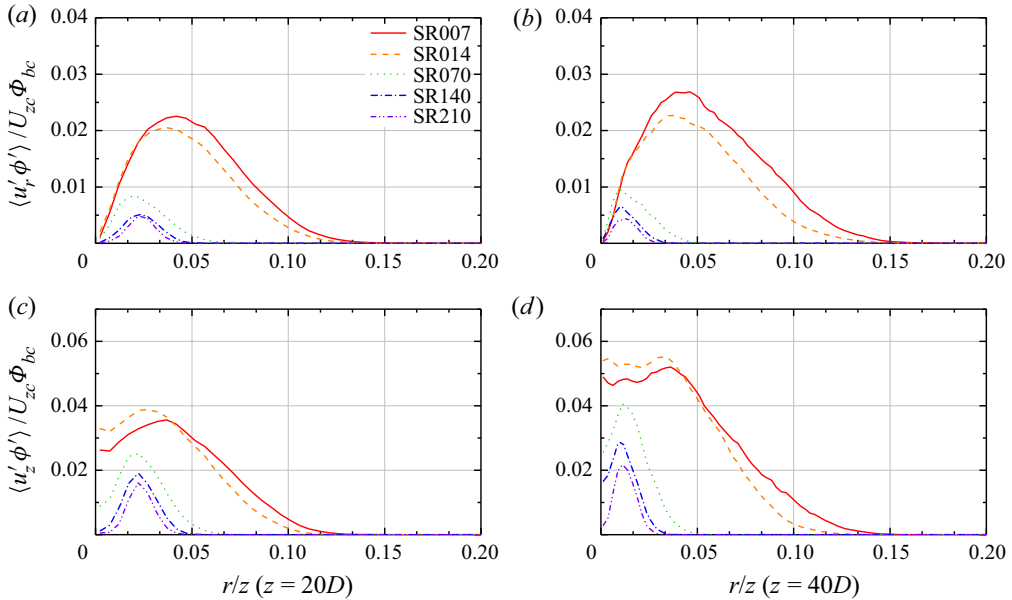
935 A4-18

Figure 13. Turbulent transportation of gas concentration toward each direction: (*a*) radial direction at $z = 20D$; (*b*) radial direction at $z = 40D$; (*c*) azimuthal direction at $z = 20D$; (*d*) azimuthal direction at $z = 40D$.

reach 0.018 as well, the peak of SR014 exceeds 0.018. This implies that there is a transition between the slip ratios of 0.14 and 0.7.

Figure 13(*a*) and 13(*b*) show the correlations between the gas concentration fluctuation and the radial velocity fluctuation. All cases have an off-centreline peak, and the smaller slip ratio shows a higher magnitude of the peak. This tendency is unlike those with other second-order turbulent characteristics in the present study, which shows that the magnitude of the second-order turbulent characteristics of SR014 is similar to that of SR007 or higher. Cases with HSR have a magnitude that is one order smaller than in the LSR cases. Also, SR007 has a peak value of 0.027, which is comparable with those of other buoyant plume cases: 0.031 (Wang & Law 2002); 0.028 (Shabbir & George 1994); and 0.02 to 0.025 (Papanicolaou & List 1988).

All cases have an off-centre peak in the near field regarding the correlation between the gas concentration fluctuation and the axial velocity fluctuation (figure 13*c*). In the far field (figure 13*d*), HSR cases still have a peak in the bubbly jet core region, but LSR cases have a flat profile in the core region. Also, SR007 shows a centreline value of 0.05 for the correlation between the gas concentration and axial velocity fluctuation, which agrees with other buoyant plume and jet results (0.05 Wang & Law 2002, 0.05 Papanicolaou & List 1988, and 0.056 Shabbir & George 1994).

Figure 14 shows the turbulent gas concentration fluctuation. Low slip ratio cases show a centre peak and collapse in the radial variation of the turbulent gas concentration fluctuation. High slip ratio cases have an off-centre peak of the gas concentration fluctuation in the bubbly jet core region. The location of the peak with HSR almost did not vary with height ($r/D \sim 0.445$), which is consistent with the location of the peak of the correlation between the gas concentration fluctuation and the velocity fluctuations.

Additionally, it is notable that the location of the peak of the turbulent shear stress is observed at $r/D \sim 0.55$, which is outside of the location of the peak of the gas
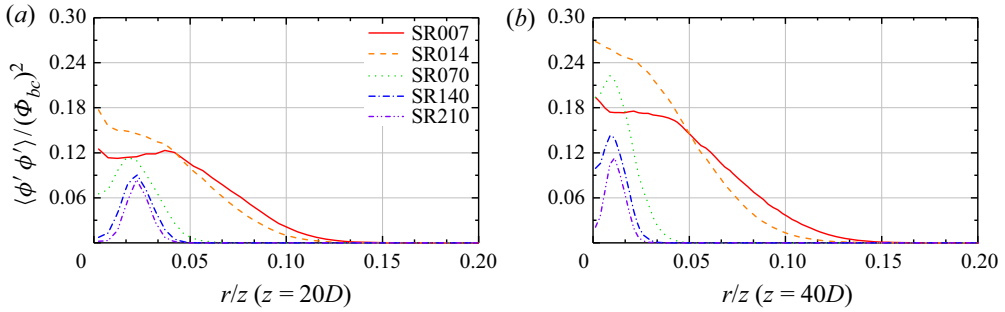
Figure 14. Turbulent gas concentration fluctuation: (*a*) turbulent gas concentration fluctuation at $z = 20D$; (*b*) turbulent gas concentration fluctuation at $z = 40D$.

concentration fluctuation. Now SR014 shows a higher magnitude of the turbulent gas concentration fluctuation than SR007. This implies that the transitional behaviour observed in second-order turbulent statistics between the slip ratios of 0.14 and 0.7 is due to the gas concentration fluctuation.

3.4. *Third-order statistics*

Third-order statistics regarding the velocity are important in terms of the contribution to the turbulent diffusion of TKE. Furthermore, third-order statistics regarding the gas concentration play a role in redistributing the gas phase with slip velocity in the flow field. Despite the long time for averaging statistics, third-order statistics do not converge in the bubbly jet core region. In the near field, all slip-ratio cases have a similar magnitude in both the radial and axial turbulent transport. But the radial variation of radial and axial turbulent transports varies with the slip ratio (figures 15*a*, 15*c*, 15*e*, 16*a*, 16*c* and 16*e*). Peaks of radial and axial turbulent transport are located at $0.04 \, r/z$–$0.07 \, r/z$. The peak with the highest slip ratio (SR210) is located at $0.04 \, r/z$, and the peak with the lowest slip ratio (SR007) is located at $0.07 \, r/z$. This range is the outer region of locations for peaks of turbulent stresses ($0.025 \, r/z$ and $0.042 \, r/z$ for the peaks of the axial normal stress and shear stress of SR210 and SR007, respectively; $0.034 \, r/z$ and $0.04 \, r/z$ for the peaks of the radial and azimuthal normal stresses of SR210 and SR007, respectively).

Each directional transport of radial and azimuthal normal stresses has a similar shape of the distribution, but the azimuthal normal stresses always show a lower magnitude of turbulent transport. Taub *et al.* (2013) reported that the radial turbulent transport of azimuthal normal stresses achieved 60 % of the triple moment of the radial velocity fluctuation in their turbulent jet case. Other studies did not quantitatively specify them but reported similar tendencies; that is, the turbulent transport of the azimuthal normal stresses had a lower magnitude than the radial normal stresses ($\langle u_\theta'^2 u_r' \rangle / \langle u_r'^3 \rangle \sim 51\,\%$ and $\langle u_\theta'^2 u_z' \rangle / \langle u_r'^2 u_z' \rangle \sim 69\,\%$ with an experiment on a heated air jet (Darisse, Lemay & Benaïssa 2015); $\langle u_\theta'^2 u_r' \rangle / \langle u_r'^3 \rangle \sim 54\,\%$ and $\langle u_\theta'^2 u_z' \rangle / \langle u_r'^2 u_z' \rangle \sim 65\,\%$ with DNS on a forced plume Taub *et al.* 2015). The present study also shows $\langle u_\theta'^2 u_r' \rangle / \langle u_r'^3 \rangle \sim 55\,\%$ and $\langle u_\theta'^2 u_z' \rangle / \langle u_r'^2 u_z' \rangle \sim 66\,\%$ in the far field ($z = 40D$).

It is notable that the radial and azimuthal normal stresses in figure 12 have similar magnitude and distribution, but the transport of the azimuthal normal stresses is lower than the radial normal stresses. On the other hand, the turbulent transport of the axial normal stress in the radial direction (figure 15*f*) is similar to the turbulent transport of the
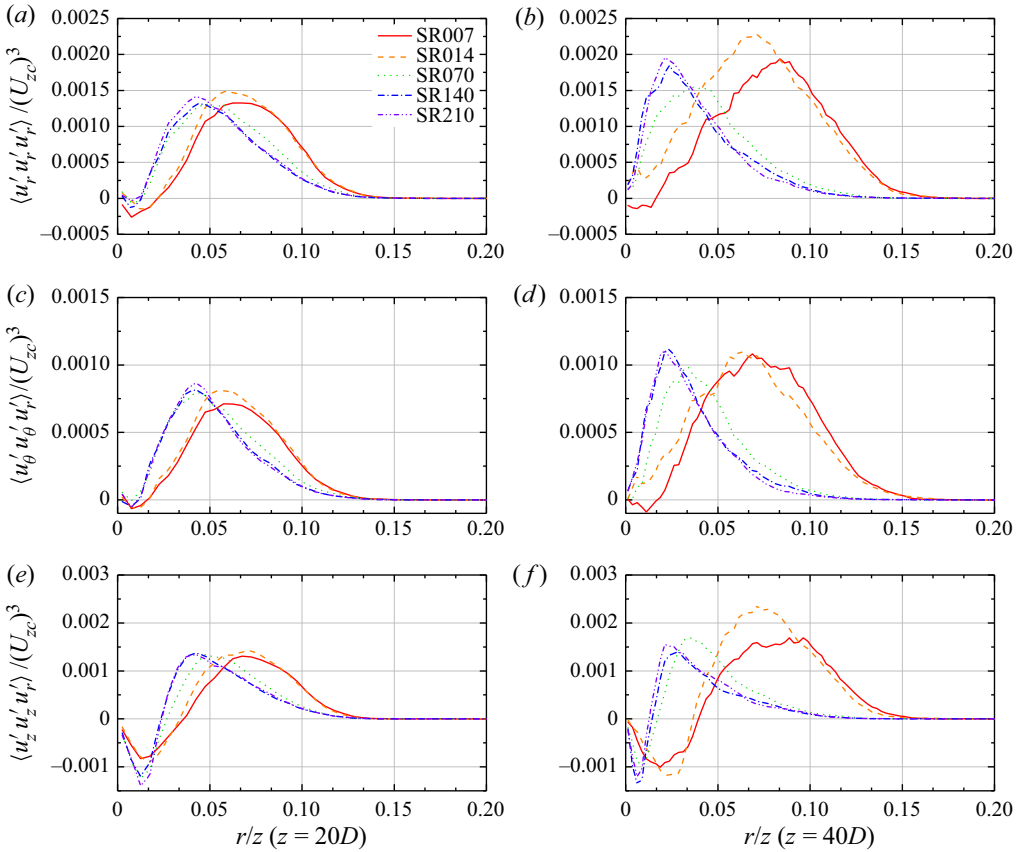
935 A4-20

Figure 15. Turbulent radial transportation of Reynolds normal stresses: (*a*) radial normal stress at $z = 20D$; (*b*) radial normal stress at $z = 40D$; (*c*) azimuthal normal stress at $z = 20D$; (*d*) azimuthal normal stress at $z = 40D$; (*e*) axial normal stress at $z = 20D$; (*f*) axial normal stress at $z = 40D$.

radial normal stress (figure 15*b*), but the turbulent transport of the axial normal stress in the axial direction (figure 16*f*) is much higher (2.5–6 times) than the other components. This fact is contrasted with the axial normal stress being just 1.5 times higher than the other components (figure 12).

Regarding the radial transport of the axial normal stress (figures 15*e*, 15*f*), all cases have a negative peak next to the centreline. The negative peak reflects that the axial Reynolds normal stress does not diffuse towards the ambient area, but the bubbly jet tends to keep its turbulent energy along the core. A preserved tendency of the TKE is also observed in the turbulent axial transport in figure 16 as negative peaks.

Correlations between the gas concentration fluctuation and Reynolds stresses are shown in figure 17. Most of the correlations near the centreline show negative values or values close to zero. This is consistent with the tendency observed in figures 15 and 16 as negative peaks in the bubbly jet core region. Correlations including the radial and azimuthal velocity components with HSRs have a very small magnitude. Meanwhile, LSR cases have a positive off-centre peak around the core region. It seems that turbulent diffusion toward the ambient area in HSR cases scarcely takes place, but prevails in LSR cases.
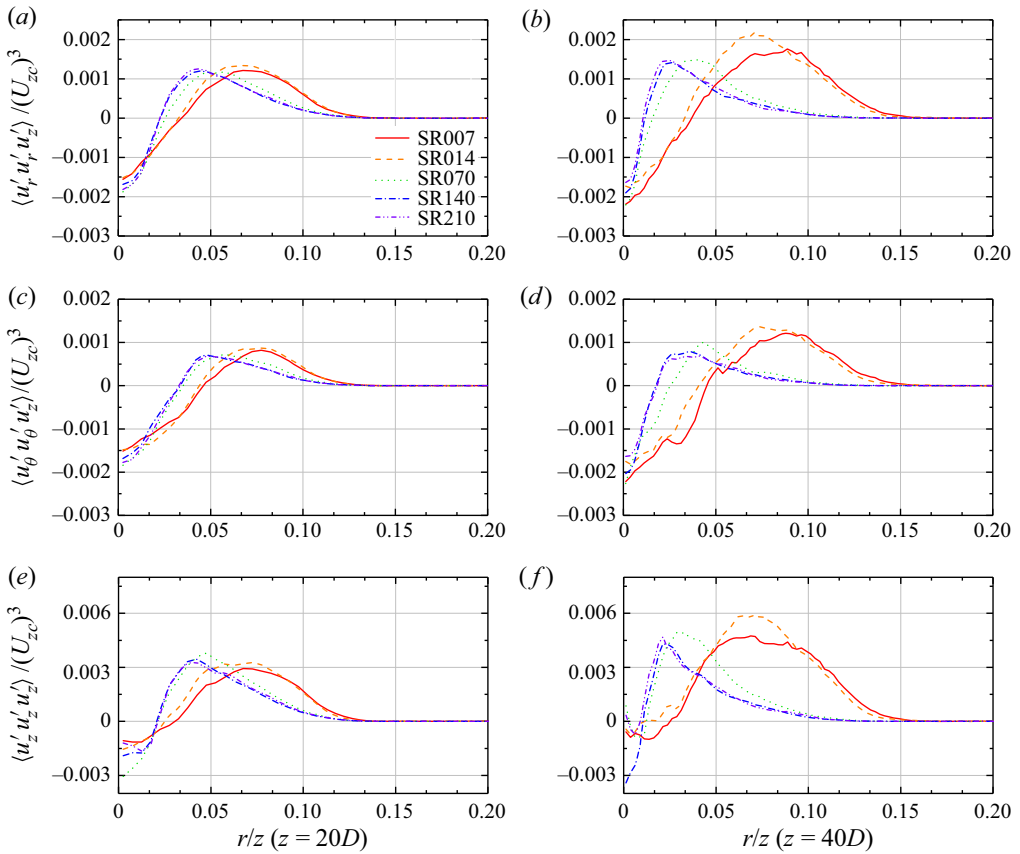
Figure 16. Turbulent axial transportation of Reynolds normal stresses: (*a*) radial normal stress at $z = 20D$; (*b*) radial normal stress at $z = 40D$; (*c*) azimuthal normal stress at $z = 20D$; (*d*) azimuthal normal stress at $z = 40D$; (*e*) axial normal stress at $z = 20D$; (*f*) axial normal stress at $z = 40D$.

The correlation between the gas concentration fluctuation and the Reynolds shear stress regularly shows a negative peak in the bubble core region and a positive peak around the bubble core for all cases (figures 17*g*, 17*h*). The magnitude of the positive peak with very HSR is not comparable to the magnitude of the LSR cases. On the other hand, the magnitude of the negative peak is comparable to the magnitude of the LSR cases. Also, the peak is located in the innermost position ($r/z - 0.008$), where the negative peak of the radial transport of the axial normal stress occurs (in other words, the axial transport of Reynolds shear stress). This implies that the fluctuation of the concentration has strong relation with the axial fluctuations in regards to the correlation with Reynolds shear stresses.

3.5. *TKE budget*

We plotted the TKE budget of the bubbly jet in the near field and far field to investigate how the bubbles contribute to the turbulent process in the bubbly jet. The transport equation of the TKE is arranged from the momentum equation and the assumption on
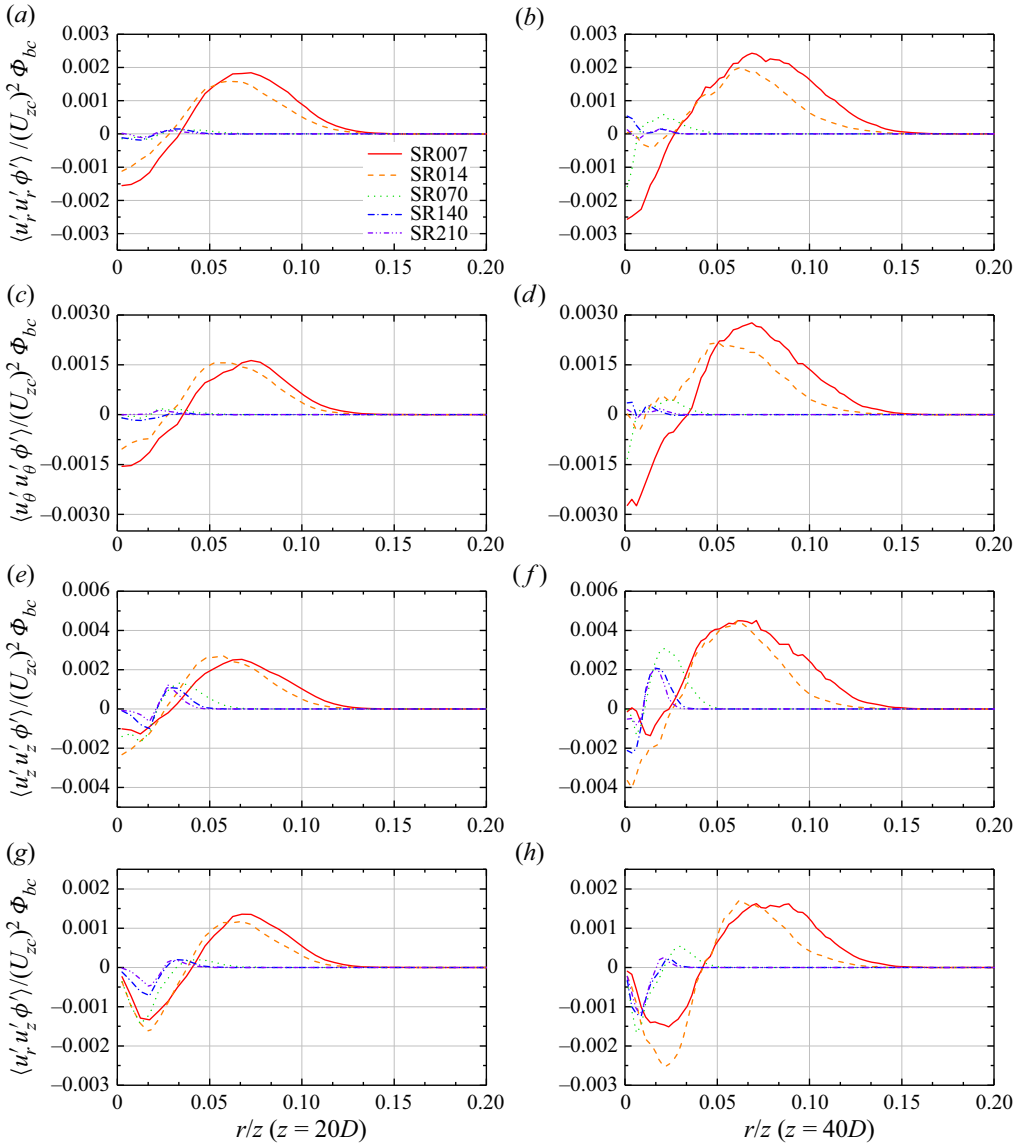
Figure 17. Correlation between gas concentration fluctuation and each Reynolds stress: (*a*) radial normal stress at $z = 20D$; (*b*) radial normal stress at $z = 40D$; (*c*) azimuthal normal stress at $z = 20D$; (*d*) azimuthal normal stress at $z = 40D$; (*e*) axial normal stress at $z = 20D$; (*f*) axial normal stress at $z = 40D$; (*g*) shear stress at $z = 20D$; (*h*) shear stress at $z = 40D$.

the axisymmetric jet flow and written as follows:

$$
0 = -\left[U_r \frac{\partial k}{\partial r} + U_z \frac{\partial k}{\partial z} \right] - \left[\frac{1}{r} \frac{\partial}{\partial r} \left(r\overline{u_r'p'} \right) + \frac{\partial}{\partial z} \left(\overline{u_z'p'} \right) \right]
$$

$$
- \left[\overline{u_r'u_r'} \frac{\partial U_r}{\partial r} + \overline{u_z'u_z'} \frac{\partial U_z}{\partial z} + \overline{u_r'u_z'} \left(\frac{\partial U_r}{\partial z} + \frac{\partial U_z}{\partial r} \right) + \frac{\overline{u_\theta'u_\theta'}U_r}{r} \right]
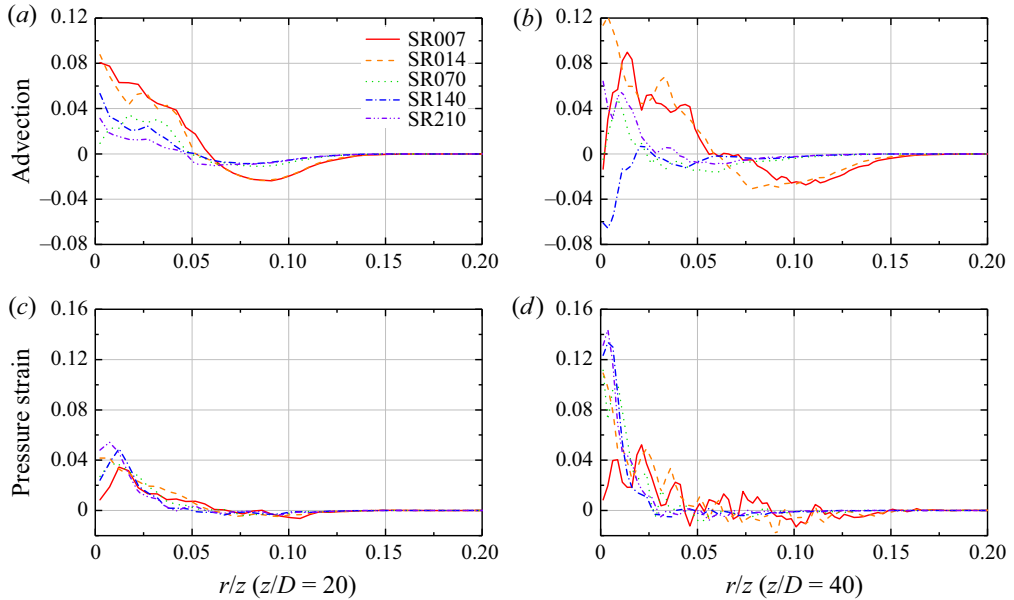$$

Figure 18. Turbulent kinetic energy budget terms at different height: (*a*) advection at $z = 20D$; (*b*) advection at $z = 40D$; (*c*) pressure strain at $z = 20D$; (*d*) pressure strain at $z = 40D$.

$$-\left[\frac{1}{r}\frac{\partial}{\partial r}\left(r\overline{u_r'k}\right) + \frac{\partial}{\partial z}\left(\overline{u_z'k}\right)\right] - \frac{1}{Re}\left[\frac{1}{r}\frac{\partial}{\partial r}\left(r\frac{\partial k}{\partial r}\right) + \frac{\partial^2 k}{\partial z^2}\right]$$

$$-\frac{1}{Re}\left[\overline{\left(\frac{\partial u_r'}{\partial r}\right)^2} + \overline{\left(\frac{\partial u_\theta'}{\partial r}\right)^2} + \overline{\left(\frac{\partial u_z'}{\partial r}\right)^2} + \overline{\left(\frac{\partial u_r'}{\partial z}\right)^2} + \overline{\left(\frac{\partial u_\theta'}{\partial z}\right)^2} + \overline{\left(\frac{\partial u_z'}{\partial z}\right)^2}\right.$$

$$\left. + \frac{\overline{u_r'u_r'}}{r^2} + \frac{\overline{u_\theta'u_\theta'}}{r^2}\right] + Ri\left[\overline{u_z'\phi_b'}\right],\tag{3.17}$$

where,

$$k = \tfrac{1}{2}\left(\overline{u_r'^2 + u_\theta'^2 + u_z'^2}\right).\tag{3.18}$$

By using the axisymmetric assumption, terms including the azimuthal differentiation, odd number of azimuthal elements and mean azimuthal velocity elements are eliminated. The terms separated by square brackets in (3.17) represent the transport of TKE by the mean flow (advection term), the transport of TKE by pressure (pressure strain term), the production by the mean shear and mean flow (production term), the transport of TKE by Reynolds stress (turbulent transport term), the transport of TKE by viscous stress (viscous transport term), the rate of dissipation (dissipation term) and the production by buoyancy (buoyancy production term). The dissipation term is obtained as a closing term of the budget. Each term is plotted in figures 18, 19 and 20. The terms are normalised by U_{zc}^3/z.

Advection and pressure strain in the bubbly jet seem to be the most unstable terms among the TKE budget terms in the present study. The advection term has a positive peak along the centreline and a negative peak around the bubbly jet core region (figure 18a). The negative peak persists in the far field. The positive peak along the centreline comes from the mean axial advection of the TKE, and the negative peak comes from entrainment
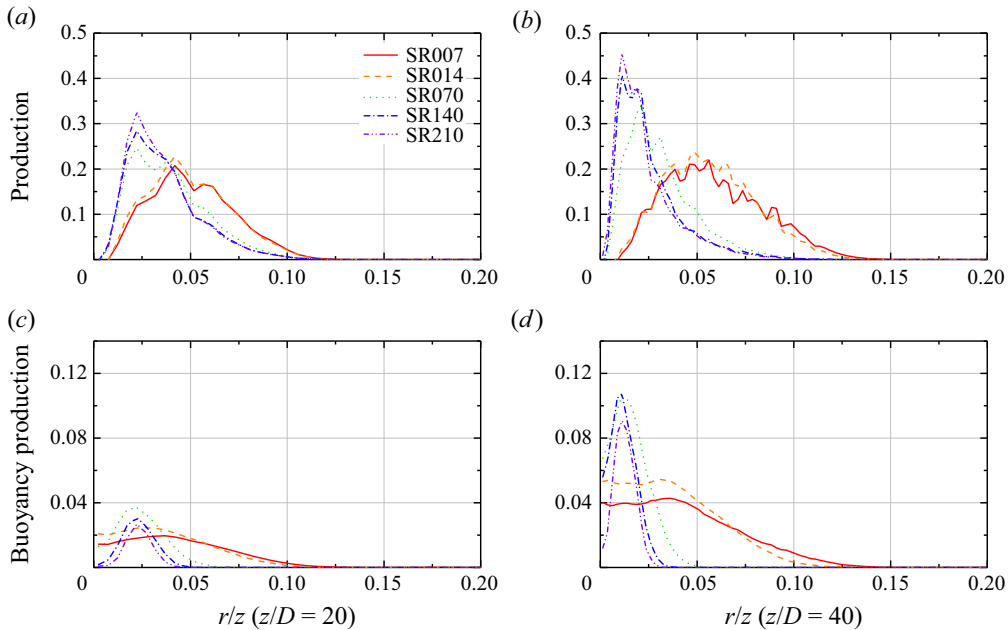
Figure 19. Turbulent kinetic energy budget terms at different height: (*a*) production at $z = 20D$; (*b*) production at $z = 40D$; (*c*) buoyancy production at $z = 20D$; (*d*) buoyancy production at $z = 40D$.

of the ambient fluid in the shear layer of the bubbly jet. But oscillations of the centreline value along the centreline are observed in figure 18(*b*). For example, SR007 and SR014, which have similar jet structure in the present study, show inconsistency in the magnitude of centreline value. Also SR210 has a negative peak in the centre of the jet, while SR070 and SR140 have a positive peak in the centre of the jet. This might come from very large spatial and temporal motion such as plume meandering (Simiano & Lakehal 2012).

As shown in figures 18(*c*) and 18(*d*), the pressure strain term of HSR cases has an off-centre peak, but the peak of the LSR cases oscillates in the far field (e.g. SR007 of figure 18*d*). The magnitude of the pressure strain in the near field is not more significant than the advection. In the far field, however, it is more dominant than the advection in HSR cases. The magnitude of the pressure strain has a distinctive peak along the centreline in the far field.

Figure 19 shows the production and buoyancy production terms. In the near field, the production is almost one order of magnitude higher than the buoyancy production. In the far field, this difference is reduced by five times. Generally, the peak of the production is observed around the bubbly jet core region and shows an accordance with the location of the peak of the buoyancy production. This is in contrast with the experimental result from a weak bubble plume, which shows a very high contribution of bubbles to the production of TKE but negligible contribution of water (Lai & Socolofsky 2019). The experiment was buoyancy dominated flow, so it resulted in low mean kinetic energy and mean shear. Therefore, its TKE production probably depends on bubble induced turbulence. Furthermore, interfacial characteristics and deformation of the bubbles can be attributed to buoyancy production in terms of pressure fluctuation and viscous forces (Nguyen *et al.* 2012; Santarelli *et al.* 2016).

Regarding the buoyancy production, LSR cases show flat radial distribution in the bubbly jet core region, and HSR cases show a peak with a non-zero centreline value.
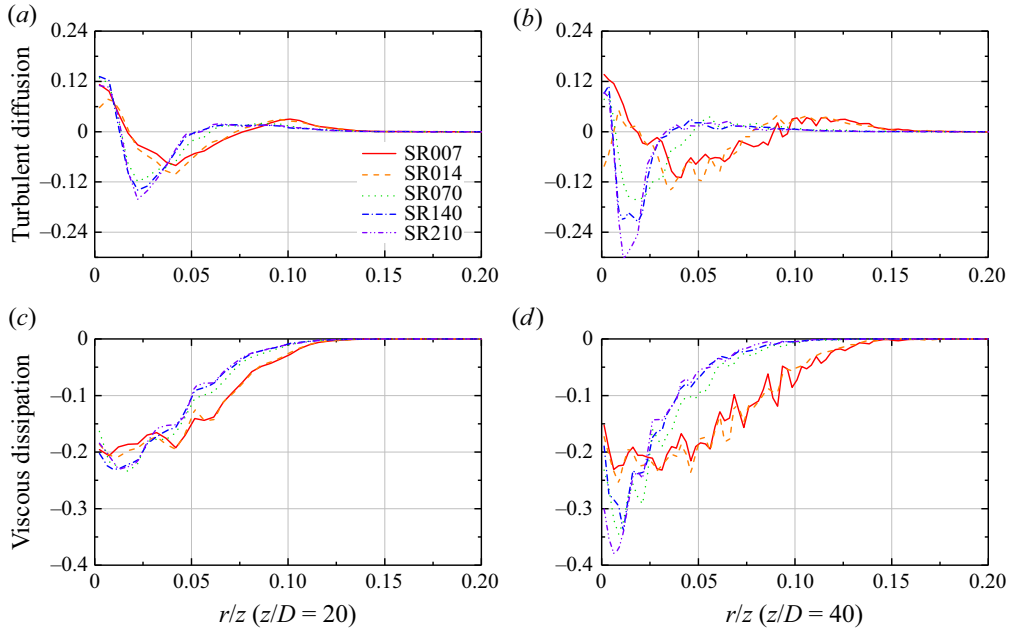
Figure 20. Turbulent kinetic energy budget terms at different height: (*a*) turbulent diffusion at $z = 20D$; (*b*) turbulent diffusion at $z = 40D$; (*c*) dissipation at $z = 20D$; (*d*) dissipation at $z = 40D$.

In the near field, all cases show similar magnitude of the buoyancy production, but LSR cases have a wider radial distribution. In the far field, the buoyancy production has two to three times higher magnitude than the magnitude in the near field. The location of the peak of SR140 and SR210 is almost in accordance with the jet concentration radius (figure 11*c*). This result shows the formation of a rigid jet core in HSR cases, and the buoyancy production takes place around the bubbly jet core interface.

Figure 20 shows the turbulent diffusion and dissipation terms. The turbulent diffusion profile typically consists of a positive peak along the centreline, a negative off-centre peak, and a very small positive peak around the shear layer of the bubbly jet. In the near field, the magnitude of the turbulent diffusion is bounded between $+0.12$ and -0.12. In the far field, there is a negative peak of around -0.24 for the HSR cases. Like the pressure strain term, LSR cases have an irregular peak along the centreline, but HSR cases regularly have a positive peak along the centreline. The distribution of the dissipation of the TKE is similar to the TKE in figure 12. Most of the dissipation occurs in the bubble core region and rapidly decreases in the outer region of the bubble core.

4. Conclusion

Bubbly jets with five different slip ratios were simulated using DNS. We chose bubble slip velocities that vary from a very small value (7 % of the inlet velocity) to a very high value (210 % of the inlet velocity). The effect of the slip velocity on the bubbly jet was studied with three different perspectives: (1) a comparison on instantaneous flow fields between HSR cases and LSR cases; (2) an integral framework with 1-D analysis; and (3) a statistical analysis with higher-order terms and the turbulent kinetic energy budget.

First of all, the single-phase jet case is validated by comparing with the literature data. After adding the gas concentration at the inlet of the bubbly jet, we found that a transition

point where the breakdown of the potential core occurs with the gas phase is observed earlier than without the gas phase. There was a negligible effect of the slip ratio on the position of the transition point, but various structural differences were observed after the transition point. High slip ratio cases keep their rigid bubbly jet core, but a gas phase with LSRs is dispersed into ambient in the form of a bubble swarm or lump.

The time-averaged spread of the gas phase was assumed to follow an exponential function that includes the slip ratio as an exponent. Ordinary differential equations regarding the axial velocity and spread of the velocity radius were derived from conservation equations with a conventional assumption about the round jets and plumes (Morton *et al.* 1956). The local entrainment coefficient was obtained from the relationship with the local Richardson number (Priestley & Ball 1955; List 1982). The axial velocity, velocity radius and gas concentration radius were predicted very well downstream of the bubbly jets.

From the analysis of the second-order statistics, it was observed that a HSR results in the prevention of diffusion of the gas phase and forms a rigid bubbly jet core along the centreline. Correlations including the gas concentration fluctuation show a peak inside the location of the peak of turbulent stresses. The normalised magnitudes of the turbulent stresses were similar in each case and comparable with those of a single-phase jet and plume in the literature. However, the distribution was narrower in HSR cases. Furthermore, the correlation between the radial velocity fluctuation and gas concentration fluctuation was severely suppressed in HSR cases. But the autocorrelation of the gas concentration fluctuation or correlations between the axial velocity fluctuation and gas concentration fluctuation were strong in the bubbly jet core region with a HSR.

From the analysis of the third-order statistics, the smallest turbulence structure of the HSR case was observed at $r/z \sim 0.008$ in the form of a negative peak of the axial transport of Reynolds shear stresses and the correlation between the Reynolds shear stress and gas concentration fluctuation. In the analysis of the TKE budget, the advection and the production terms showed similar distributions to what was observed in conventional jets and plumes. However, turbulent diffusion and pressure strain terms showed a positive peak along the centreline, which was not reported for single-phase jets and plumes. The buoyancy production generated by bubbles is two to three times more dominant in the far field than in the near field.

Declaration of interests. The authors report no conflict of interest.

Author ORCIDs.

Hyunduk Seo https://orcid.org/0000-0002-9011-919X;

S. Balachandar https://orcid.org/0000-0003-3619-3695;

Kyung Chun Kim https://orcid.org/0000-0002-7943-9774.

Appendix A

In this appendix, we derive the ordinary differential equations for the jet centreline velocity and jet velocity radius. These properties are derived from conservation equations for round jets and plumes regarding the volume flux, momentum flux and buoyancy flux. In fully developed flows, the buoyancy flux F_G is constant under the Boussinesq approximation

and can be expressed with the inlet buoyancy flux F_{G0} as

$$F_{G0} = Q_{g0}g'. \tag{A1}$$

Here, Q_{g0} is the volume flux of the gas phase at the source. The general form of the buoyancy flux with the Gaussian profile assumption is expressed in (3.8). You can find overlapped expressions $(\pi g' \Phi_{bc}(\lambda b)^2)$ in (3.8) and (3.10). The right-hand side of (3.10) can replace the same expression in (3.8), i.e.

$$F(z) = F_{G0} = Q_{g0}g'$$
$$= \frac{\pi}{2}\frac{d}{dz}(U_{zc}^2 b^2)\left(\frac{U_{zc}}{1+\lambda^2} + u_{sr}\right). \tag{A2}$$

This equation can be rearranged by putting the derivative term on the left-hand side, i.e.

$$\frac{d}{dz}(U_{zc}^2 b^2) = \frac{2}{\pi}\frac{Q_{g0}g'}{U_{zc}/(1+\lambda^2) + u_{sr}}. \tag{A3}$$

For further derivation, we should recall continuity equation (3.9), namely

$$\frac{d(\pi U_{zc}b^2)}{dz} = 2\pi\alpha U_{zc}b. \tag{A4}$$

By the product rule of the derivative, (A3) can be separated into two parts of the derivatives, as follows:

$$\frac{d}{dz}(U_{zc}^2 b^2) = \frac{d}{dz}(U_{zc})(U_{zc}b^2) + \frac{d}{dz}(U_{zc}b^2)(U_{zc}), \tag{A5}$$

where $d(U_{zc}b^2)/dz$ is already known as (A4). Then, the equation can be rearranged for $d(U_{zc})/d(z)$ as follows:

$$\frac{d}{dz}(U_{zc}) = \left[-U_{zc}\frac{d}{dz}(U_{zc}b^2) + \frac{d}{dz}(U_{zc}^2 b^2)\right]/(U_{zc}b^2). \tag{A6}$$

This equation is the same as (3.13). In the same way, $d(b)/dz$ can be expressed as follows:

$$\frac{d}{dz}(b) = \left[\frac{d}{dz}(U_{zc}b^2) - \frac{d}{dz}(U_{zc}b)b\right]/(U_{zc}b)$$
$$= \left[\frac{d}{dz}(U_{zc}b^2) - \frac{d}{dz}(U_{zc}^2 b^2)/(2U_{zc}b)\right]/(U_{zc}b)$$
$$= 2\alpha - \frac{Q_{g0}g'}{\pi U_{zc}^2 b(U_{zc}/(1+\lambda^2) + u_{sr})}. \tag{A7}$$

REFERENCES

AKIKI, G., MOORE, W.C. & BALACHANDAR, S. 2017 Pairwise-interaction extended point-particle model for particle-laden flows. *J. Comput. Phys.* **351**, 329–357.

ALMÉRAS, E., PLAIS, C., EUZENAT, F., RISSO, F., ROIG, V. & AUGIER, F. 2016 Scalar mixing in bubbly flows: experimental investigation and diffusivity modelling. *Chem. Engng Sci.* **140**, 114–122.

ASAEDA, T. & IMBERGER, J. 1993 Structure of bubble plumes in linearly stratified environments. *J. Fluid Mech.* **249**, 35–57.

BECKER, H.A. & MASSARO, T.A. 1968 Vortex evolution in a round jet. *J. Fluid Mech.* **31** (3), 435–448.

BOERSMA, B.J., BRETHOUWER, G. & NIEUWSTADT, F.T.M. 1998 A numerical investigation on the effect of the inflow conditions on the self-similar region of a round jet. *Phys. Fluids* **10** (4), 899–909.

BRYANT, D.B., SEOL, D.G. & SOCOLOFSKY, S.A. 2009 Quantification of turbulence properties in bubble plumes using vortex identification methods. *Phys. Fluids* **21** (7), 075101.

BUSCAGLIA, G.C., BOMBARDELLI, F.A. & GARCÍA, M.H. 2003 Numerical modeling of large-scale bubble plumes accounting for mass transfer effects. *Intl J. Multiphase Flow* **28** (11), 1763–1785.

CHEN, C.J. & NIKITOPOULOS, C.P. 1979 On the near field characteristics of axisymmetric turbulent buoyant jets in a uniform environment. *Intl J. Heat Mass Transfer* **22** (2), 245–255.

COMBEST, D.P., RAMACHANDRAN, P.A. & DUDUKOVIC, M.P. 2011 On the gradient diffusion hypothesis and passive scalar transport in turbulent flows. *Ind. Engng Chem. Res.* **50** (15), 8817–8823.

DARISSE, A., LEMAY, J. & BENAÏSSA, A. 2015 Budgets of turbulent kinetic energy, Reynolds stresses, variance of temperature fluctuations and turbulent heat fluxes in a round jet. *J. Fluid Mech.* **774**, 95–142.

DITMARS, J.D. & CEDERWALL, K. 1974 Analysis of air-bubble plumes. In *Proceedings of the 14th Conference on Coastal Engineering, Copenhagen, Denmark*, pp. 2209–2226. ASCE.

DU CLUZEAU, A., BOIS, G. & TOUTANT, A. 2019 Analysis and modelling of Reynolds stresses in turbulent bubbly up-flows from direct numerical simulations. *J. Fluid Mech.* **866**, 132–168.

EL KHOURY, G.K., SCHLATTER, P., NOORANI, A., FISCHER, P.F., BRETHOUWER, G. & JOHANSSON, A.V. 2013 Direct numerical simulation of turbulent pipe flow at moderately high Reynolds numbers. *Flow Turbul. Combust.* **91** (3), 475–495.

EVANS, J.T. 1955 Pneumatic and similar breakwaters. *Proc. R. Soc. Lond.* A **231** (1187), 457–466.

FABREGAT, A., DEWAR, W.K., OZGOKMEN, T.M., POJE, A.C. & WIENDERS, N. 2015 Numerical simulations of turbulent thermal, bubble and hybrid plumes. *Ocean Model.* **90**, 16–28.

FABREGAT, A., POJE, A.C., ÖZGÖKMEN, T.M. & DEWAR, W.K. 2016 Dynamics of multiphase turbulent plumes with hybrid buoyancy sources in stratified environments. *Phys. Fluids* **28** (9), 095109.

FERDMAN, E., ÖTÜGEN, M.V. & KIM, S. 2000 Effect of initial velocity profile on the development of round jets. *J. Propul. Power* **16** (4), 676–686.

FISCEHR, H.B., LIST, E.J., KOH, R.C.Y., IMBERGER, J. & BROOKS, N.H. 1979 Chapter 9. Turbulent jets and plumes. In *Mixing in Inland and Coastal Waters* (ed. H.B. Fischer, E. John List, R.C.Y. Koh, J. Imberger & N.H. Brooks), pp. 315–389. Academic Press.

FISCHER, P.F., LOTTES, J.W. & KERKEMEIER, S.G. 2008 NEK5000 solver. http://nek5000.mcs.anl.gov.

FRAGA, B. & STOESSER, T. 2016 Influence of bubble size, diffuser width, and flow rate on the integral behavior of bubble plumes. *J. Geophys. Res.* **121**, 3887–3904.

GEORGE, W.K. 1989 The self-preservation of turbulent flows an its relation to initial conditions and coherent structures. In *Advances in Turbulence*, pp. 39–73. CRC Press.

HENDERSON-SELLERS, B. 1983 The zone of flow establishment for plumes with significant buoyancy. *Appl. Math. Model.* **7** (6), 395–398.

INCE, S. 1964 A guide to the design of air bubblers for melting ice. In *Proceedings of the 9th Conference on Coastal Engineering, Lisbon*, pp. 600–610. ASCE.

JEONG, J. & HUSSAIN, F. 1995 On the identification of a vortex. *J. Fluid Mech.* **285**, 69–94.

JOBEHDAR, M.H., SIDDIQUI, K., GADALLAH, A.H. & CHISHTY, W.A. 2016 Bubble formation process from a novel nozzle design in liquid cross-flow. *Intl J. Heat Fluid Flow* **61**, 599–609.

KOBUS, H. 1968 Analysis of the flow induced by air-bubble systems. *Proceedings of the 11th Conference on Coastal Engineering, London*, pp. 1016–1031. ASCE.

LAI, C.C.K. & SOCOLOFSKY, S.A. 2019 The turbulent kinetic energy budget in a bubble plume. *J. Fluid Mech.* **865**, 993–1041.

LIMA NETO, I.E. 2015 Self-similarity of vertical bubbly jets. *Braz. J. Chem. Engng* **32** (2), 475–487.

LIMA NETO, I.E., ZHU, D.Z. & RAJARATNAM, N. 2008 Bubbly jets in stagnant water. *Intl J. Multiphase Flow* **34** (12), 1130–1141.

LIST, E.J. 1982 Turbulent jets and plumes. *Annu. Rev. Fluid Mech.* **14** (1), 189–212.

MCDOUGALL, T.J. 1978 Bubble plumes in stratified environments. *J. Fluid Mech.* **85** (Apr), 655–672.

MILGRAM, J.H. 1983 Mean flow in round bubble plumes. *J. Fluid Mech.* **133**, 345–376.

MORTON, B.R., TAYLOR, G. & TURNER, J.S. 1956 Turbulent gravitational convection from maintained and instantaneous sources. *Proc. R. Soc. Lond.* A **234** (1196), 1–23.

NGUYEN, V.T., BAE, B.U., EUH, D.J., SONG, C.H. & YUN, B.J. 2012 The effect of bubble-induced turbulence on the interfacial area transport in gas-liquid two-phase flow. *J. Comput. Multiphase Flows* **4** (3), 327–340.

PANCHAPAKESAN, N.R. & LUMLEY, J.L. 1993 Turbulence measurements in axisymmetric jets of air and helium. Part 2. Helium Jet. *J. Fluid Mech.* **246**, 225–247.

PAPANICOLAOU, P.N. & LIST, E.J. 1988 Investigations of round vertical turbulent buoyant jets. *J. Fluid Mech.* **195**, 341–391.

PRIESTLEY, C.H.B. & BALL, F.K. 1955 Continuous convection from an isolated source of heat. *Q. J. R. Meteorol. Soc.* **81** (348), 144–157.

REDDY, R.K., SATHE, M.J., JOSHI, J.B., NANDAKUMAR, K. & EVANS, G.M. 2013 Recent developments in experimental (PIV) and numerical (DNS) investigation of solid-liquid fluidized beds. *Chem. Engng Sci.* **92**, 1–12.

REICHARDT, T., TRYGGVASON, G. & SOMMERFELD, M. 2017 Effect of velocity fluctuations on the rise of buoyant bubbles. *Comput. Fluids* **150**, 8–30.

RODI, W. 1975 A new method of analysing hot-wire signals in highly turbulent flow, and its evaluation in a round jet. *DISA Inf.* **17**, 9–18.

SALEHIPOUR, H., PELTIER, W.R. & MASHAYEK, A. 2015 Turbulent diapycnal mixing in stratified shear flows: the influence of Prandtl number on mixing efficiency and transition at High Reynolds number. *J. Fluid Mech.* **773**, 178–223.

SANTARELLI, C., ROUSSEL, J. & FRÖHLICH, J. 2016 Budget analysis of the turbulent kinetic energy for bubbly flow in a vertical channel. *Chem. Engng Sci.* **141**, 46–62.

SARIKURT, F.S. & HASSAN, Y.A. 2017 Large eddy simulations of erosion of a stratified layer by a buoyant jet. *Intl J. Heat Mass Transfer* **112**, 354–365.

SCHMIDT, W. 1941 Turbulent propagation of a stream of heated air. *Z. Angew. Math. Mech.* **21**, 265–278.

SEO, H. & KIM, K.C. 2021 Experimental study on flow and turbulence characteristics of bubbly jet with low void fraction. *Intl J. Multiphase Flow* **142**, 103738.

SEOL, D.-G., BHAUMIK, T., BERGMANN, C. & SOCOLOFSKY, S.A. 2007 Particle image velocimetry measurements of the mean flow characteristics in a bubble plume. *J. Engng Mech.* **133** (6), 665–676.

SHABBIR, A. & GEORGE, W.K. 1994 Experiments on a round turbulent buoyant plume. *J. Fluid Mech.* **275**, 1–32.

SHAH, Y.T., KELKAR, B.G., GODBOLE, S.P. & DECKWER, W.-D. 1982 Design parameters estimations for bubble column reactors. *AIChE J.* **28** (3), 353–379.

SIMIANO, M. & LAKEHAL, D. 2012 Turbulent exchange mechanisms in bubble plumes. *Intl J. Multiphase Flow* **47**, 141–149.

SOCOLOFSKY, S.A. & ADAMS, E.E. 2005 Role of slip velocity in the behavior of stratified multiphase plumes. *J. Hydraul. Engng* **131** (4), 273–282.

SOKOLICHIN, A., EIGENBERGER, G. & LAPIN, A. 2004 Simulation of buoyancy driven bubbly flow: established simplifications and open questions. *AIChE J.* **50** (1), 24–45.

SUN, T.Y. & FAETH, G.M. 1986 Structure of turbulent bubbly jets – II. Phase property profiles. *Intl J. Multiphase Flow* **12** (1), 115–126.

TAMMISOLA, O. & JUNIPER, M.P. 2016 Coherent structures in a swirl injector at $Re = 4800$ by nonlinear simulations and linear global modes. *J. Fluid Mech.* **792**, 620–657.

TAUB, G.N., LEE, H., BALACHANDAR, S. & SHERIF, S.A. 2013 A direct numerical simulation study of higher order statistics in a turbulent round jet. *Phys. Fluids* **25** (11).

TAUB, G.N., LEE, H., BALACHANDAR, S. & SHERIF, S.A. 2015 An examination of the high-order statistics of developing jets, lazy and forced plumes at various axial distances from their source. *J. Turbul.* **16** (10), 950–978.

TAYLOR, G.I. 1955 The action of a surface current used as a breakwater. *Proc. R. Soc. Lond.* A **231** (1187), 466–478.

TERASAKA, K., HIRABAYASHI, A., NISHINO, T., FUJIOKA, S. & KOBAYASHI, D. 2011 Development of microbubble aerator for waste water treatment using aerobic activated sludge. *Chem. Engng Sci.* **66** (14), 3172–3179.

TOMINAGA, Y. & STATHOPOULOS, T. 2007 Turbulent Schmidt numbers for CFD analysis with various types of flowfield. *Atmos. Environ.* **41** (37), 8091–8099.

WANG, B., LAI, C.C.K. & SOCOLOFSKY, S.A. 2019 Mean velocity, spreading and entrainment characteristics of weak bubble plumes in unstratified and stationary water. *J. Fluid Mech.* **874**, 102–130.

WANG, H.W. & LAW, A.W.K. 2002 Second-order integral model for a round turbulent buoyant jet. *J. Fluid Mech.* **459**, 397–428.

WU, F., LUO, K. & FAN, J. 2016 DNS of a turbulent flow past two fully resolved aligned spherical particles. *Adv. Powder Technol.* **27** (4), 1149–1161.

WÜEST, A., BROOKS, N.H. & IMBODEN, D.M. 1992 Bubble plume modeling for lake restoration. *Water Resour. Res.* **28** (12), 3235–3250.

WYGNANSKI, I. & FIEDLER, H. 1969 Some measurements in the self-preserving jet. *J. Fluid Mech.* **38** (3), 577–612.

YANG, D., CHEN, B.C., SOCOLOFSKY, S.A., CHAMECKI, M. & MENEVEAU, C. 2016 Large-eddy simulation and parameterization of buoyant plume dynamics in stratified flow. *J. Fluid Mech.* **794**, 798–833.

ZHANG, J.P., GRACE, J.R., EPSTEIN, N. & LIM, K.S. 1997 Flow regime identification in gas-liquid flow and three-phase fluidized beds. *Chem. Engng Sci.* **52** (21–22), 3979–3992.